RESEARCH ARTICLE

Structural insights into the activation of human calcium-sensing receptor

Xiaochen Chen[1†], Lu Wang[1†], Qianqian Cui[1†], Zhanyu Ding[1†], Li Han[1], Yongjun Kou[1], Wenqing Zhang[1], Haonan Wang[1], Xiaomin Jia[1], Mei Dai[1], Zhenzhong Shi[1], Yuying Li[1], Xiyang Li[1], Yong Geng[1,2*]

[1]The CAS Key Laboratory of Receptor Research, Shanghai Institute of Materia Medica, Chinese Academy of Sciences, Shanghai, China; [2]University of Chinese Academy of Sciences, Beijing, China

Abstract Human calcium-sensing receptor (CaSR) is a G-protein-coupled receptor that maintains Ca^{2+} homeostasis in serum. Here, we present the cryo-electron microscopy structures of the CaSR in the inactive and agonist+PAM bound states. Complemented with previously reported structures of CaSR, we show that in addition to the full inactive and active states, there are multiple intermediate states during the activation of CaSR. We used a negative allosteric nanobody to stabilize the CaSR in the fully inactive state and found a new binding site for Ca^{2+} ion that acts as a composite agonist with L-amino acid to stabilize the closure of active Venus flytraps. Our data show that agonist binding leads to compaction of the dimer, proximity of the cysteine-rich domains, large-scale transitions of seven-transmembrane domains, and inter- and intrasubunit conformational changes of seven-transmembrane domains to accommodate downstream transducers. Our results reveal the structural basis for activation mechanisms of CaSR and clarify the mode of action of Ca^{2+} ions and L-amino acid leading to the activation of the receptor.

***For correspondence:** gengyong@simm.ac.cn

†These authors contributed equally to this work

Competing interest: The authors declare that no competing interests exist.

Funding: See page 20

Received: 19 March 2021
Preprinted: 31 March 2021
Accepted: 31 August 2021
Published: 01 September 2021

Reviewing Editor: Randy B Stockbridge, University of Michigan, United States

Introduction

Extracellular calcium ions (Ca^{2+}) are required for various kinds of biological processes in the human body. Human calcium-sensing receptor (CaSR) is a G-protein-coupled receptor (GPCR) that senses small fluctuations of extracellular levels of Ca^{2+} ions in the blood (***Brown et al., 1993***). It maintains Ca^{2+} homeostasis by the modulation of parathyroid hormone (PTH) secretion from parathyroid cells and the regulation of Ca^{2+} reabsorption by the kidney (***Brown, 2013***). Recently, it has been reported that CaSR is also a phosphate sensor that can sense moderate changes in extracellular phosphate concentration (***Centeno et al., 2019***; ***Chang et al., 2020***; ***Geng et al., 2016***). Dysfunctions of CaSR or mutations in its genes may lead to Ca^{2+} homeostatic disorders, such as familial hypocalciuric hypercalcemia, neonatal severe hyperparathyroidism, and autosomal dominant hypocalcemia (***Hendy et al., 2009***; ***Pollak et al., 1993***; ***Ward et al., 2012***).

CaSR belongs to the family C GPCR that includes gamma-aminobutyric acid B ($GABA_B$) receptors, metabotropic glutamate receptors (mGluRs), taste receptors, GPRC6a, and several orphan receptors (***Ellaithy et al., 2020***; ***Hannan et al., 2018***; ***Heaney and Kinney, 2016***; ***Pin and Bettler, 2016***). Like most class C GPCRs, CaSR functions as a disulphide-linked homodimer. Each subunit of CaSR is comprised of a large extracellular domain (ECD) that contains a ligand-binding Venus flytrap (VFT) domain and a cysteine rich domain (CRD), and a seven-transmembrane domain (7TMD) that connects to CRD to carry signals from VFT domain to downstream G proteins (***Geng et al., 2016***; ***Zhang et al., 2016***).

CaSR can be activated or modulated by Ca^{2+} ions, amino acids (***Geng et al., 2016***; ***Liu et al., 2020***; ***Zhang et al., 2016***), L-1,2,3,4-tetrahydronorharman-3-carboxylic acid (TNCA), a tryptophan derivative ligand (***Zhang et al., 2016***), and several commercial calcium mimetic drugs, such as cinacalcet (***Leach et al., 2016***; ***Nemeth et al., 2004***), etelcalcetide, and evocalcet (positive allosteric modulator, PAM,

of CaSR) that are used for patients with end-stage kidney diseases undergoing dialysis (***Alexander et al., 2015***; ***Leach et al., 2016***; ***Walter et al., 2013***).

Recent groundbreaking structural studies of several full-length class C receptors, such as mGluR5 (***Koehl et al., 2019***) and $GABA_B$ receptors (***Kim et al., 2020***; ***Mao et al., 2020***; ***Papasergi-Scott et al., 2020***; ***Park et al., 2020***; ***Shaye et al., 2020***), by cryo-electron microscopy (cryo-EM) have provided a structural framework to unravel the activation mechanisms of class C GPCRs. The crystal structures of the resting and active conformations of CaSR ECD were solved by two different groups (***Geng et al., 2016***; ***Zhang et al., 2016***). More recently, Ling et al. have solved the cryo-EM structures of full-length CaSR in active and inactive states; however, their inactive structures do not show the fully inactive state and exhibit some characteristics of the active conformation of crystal CaSR ECD (***Ling et al., 2021***; ***Geng et al., 2016***). In their active structures, they proposed that Ca^{2+} ions and L-Trp work cooperatively to activate CaSR, leading to the closure of VFT domain.

In our study, we used cryo-EM to obtain the structures of full-length CaSR in inactive and agonist+PAM bound conformations. The fully inactive structure is stabilized by a negative allosteric nanobody. In the agonist+PAM bound structure, we identified a new calcium binding site at the inter-domain cleft of VFT, with Ca^{2+} and TNCA constitute a composite agonist to stabilize the closure of the VFT, leading to the conformational changes of the 7TMDs to initiate signaling.

Results

Identification of camelid nanobodies stabilizing the inactive state of CaSR

For structural studies, we used nanobody to stabilize CaSR in the inactive conformation. Published structures of CaSR-ECD demonstrate that agonist binding induces conformational changes of VFT

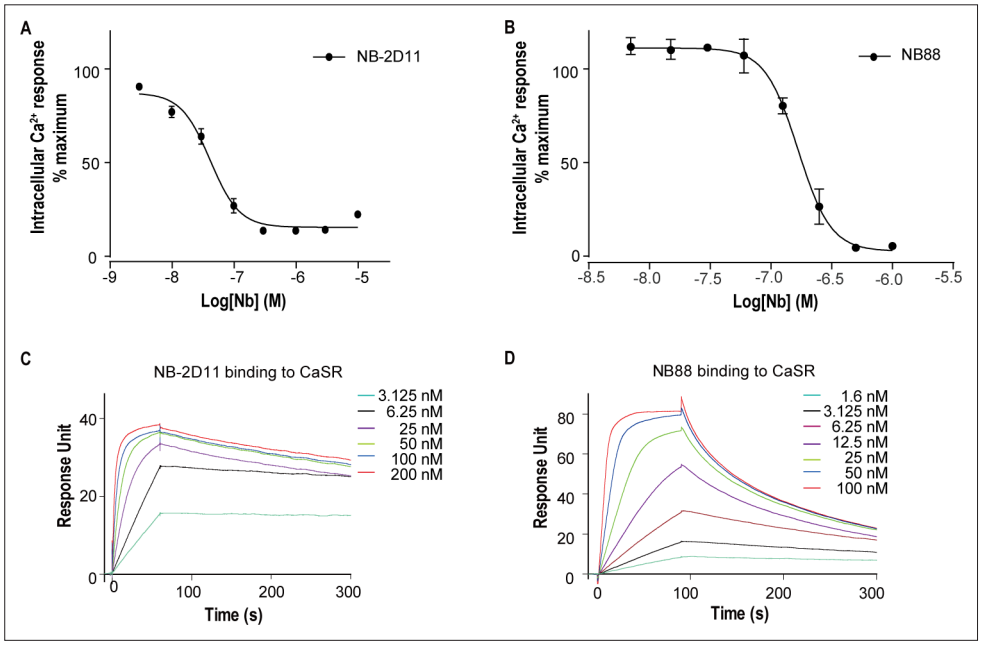

Figure 1. The function and binding affinity of NB-2D11 and NB88. (**A**) Dose-dependent NB-2D11-inhibited intracellular Ca^{2+} mobilization in response to Ca^{2+} ions. N = 3, data represent mean ± SEM (***Figure 1—source data 1***). (**B**) Dose-dependent NB-88-inhibited intracellular Ca^{2+} mobilization in response to Ca^{2+} ions. N = 3, data represent mean ± SEM (***Figure 1—source data 1***). (**C**) SPR sensorgram showing that NB-2D11 bound to CaSR with 0.24 nM affinity (***Figure 1—source data 2***). (**D**) SPR sensorgram showing that NB88 bound to CaSR with 3.9 nM affinity (***Figure 1—source data 2***).

The online version of this article includes the following figure supplement(s) for figure 1:

Source data 1. Intracellular Ca^{2+} flux assay on CaSR-NB-2D11 and CaSR-NB88 complex.

Source data 2. SPR sensorgram of NB-2D11 and NB88 binding affinity.

model of CaSR, whereby two separate LB2 domains approach each other, forming a novel interface in the active state (***Geng et al., 2016***). Based on these structural information, we introduced a potential N-linked glycosylation site on the contacting interface between LB2 domains in the active CaSR to block the interaction of LB2 domains and keep the CaSR in an inactive state. We made a double mutation R227N-E229S at the dimer interface of LB2 domain to introduce N-linked glycosylation at 227 residues site. We immunized two camels with the mutant of CaSR and generated nanobody phage display library. We performed two rounds of bio-panning on the mutant of CaSR and used enzyme-linked immunosorbent assay (ELISA) to verify the nanobodies that specifically bound to CaSR. We performed intracellular Ca^{2+} flux assay to determine whether screened nanobodies could stabilize CaSR in the inactive state. Of the several CaSR binders, NB-2D11 and NB88 significantly inhibited the activity of CaSR with IC_{50} of 41.7 nM and 167.1 nM, respectively (***Figure 1A,B***). Using surface plasmon resonance (SPR) to measure binding kinetics, both nanobodies NB-2D11 and NB88 demonstrated high-affinity binding to CaSR with K_D of 0.24 nM and 3.9 nM, respectively (***Figure 1C,D***). We then selected NB-2D11, which has a greater binding affinity of the two nanobodies, for structural study.

Determining the cryo-EM structures of full-length CaSR

To obtain the structure of the receptor in the agonist+PAM bound state, we collected a dataset of detergent solubilized full-length CaSR in the presence of PAM cinacalcet, 10 mM calcium and the compound TNCA. We have observed two active conformations with overall resolutions of 2.99 Å and 3.43 Å (***Figure 2—figure supplement 1***). We performed local refinement of ECDs and TMDs separately to obtain maps with resolutions of 3.07 Å and 4.3 Å, respectively, with quality density throughout (***Figure 2—figure supplement 1A***; ***Table 1***). The high-quality density maps present well-solved features in the ECD, which allow the unambiguous assignment of calcium, TNCA, and most side chains of amino acids of the receptor (***Figure 2A,C***, ***Figure 2—figure supplement 2***). Despite low local resolution of 7TMD, we were able to define the backbone of TM helices and even side chains of some amino acids (***Figure 2C***, ***Figure 2—figure supplement 3A***).

To stabilize the structure of CaSR in the inactive state, we collected a dataset of CaSR in glycodiosgenin (GDN) formed micelles in the presence of NPS-2143 (a negative allosteric modulator, NAM) and the inhibitory nanobody (NB-2D11). Cryo-EM data present three conformations of inactive CaSR with an overall resolution of 5.79 Å, 6.88 Å, and 7.11 Å, respectively (***Figure 2—figure supplement 4***). The local refinement focusing on the ECDs and the 7TMDs was performed separately to improve the resolutions to 4.5 Å and 4.8 Å, respectively, with quality density throughout (***Figure 2—figure supplement 4A***; ***Table 1***), which enabled us to confidently build the backbone of the inactive CaSR model (***Figure 2D***, ***Figure 2—figure supplement 3B***).

The overall structures in the inactive and agonist+PAM bound states are homodimeric arrangement, in which two subunits almost parallelly interact in a side-by-side manner while facing opposite directions. For each subunit, the VFT domain is linked to the canonical 7TMD via CRD, which is almost perpendicular to the bilayer membranes (***Figure 2B,D***). The agonist+PAM bound structure of CaSR displays a substantial compaction compared to the inactive structure, including the reduction of length, height, and width. Moreover, their width changed most obviously because there are four interfaces with interaction between the two protomers at each of LB1 domain, LB2 domain, CRD, and 7TM domains (***Figure 2***), both VFT modules adopt closed–closed conformation, and the TNCA and Ca^{2+} ion composite is bound at the interdomain cleft between LB1 domain and LB2 domain (***Figures 2C and 3A***). The closure of the VFT is relayed to TMD through the interaction of the intersubunit CRD. The overall conformation of our agonist+PAM bound structure is consistent with the recently reported active conformation of the Ca^{2+}/L-Trp-bound structure of CaSR ($CaSR^{Acc}$) (***Ling et al., 2021***; ***Figure 2—figure supplement 5A–D***).

In the inactive structure, there is only one interface at the apex of the receptor and the VFT module adopts an open conformation with the nanobody binding at the left lateral side of each LB2 domain (***Figure 2B,D***). The active state has the overall buried surface area of 3378 $Å^2$, whereas it substantially decreases to 1346 $Å^2$ in the inactive state (***Figure 2—figure supplement 3C,D***). Ling et al. recently published three different structures of CaSR in the inactive state, in which the VFT module adopted closed–closed, open–closed, and open–open conformations. However, due to low resolution, they only built the structure of CaSR in the inactive closed–closed conformation ($CaSR^{Icc}$). Comparing our inactive open–open conformation ($CaSR^{fully\ inactive}$) with their $CaSR^{Icc}$ revealed similar 7TM domains, but

Table 1. Cryo-EM data collection, refinement, and validation statistics.

CaSR	#1 inactive (EMD-30997) (PDB 7E6U)	#2 agonist+PAM (EMD-30996) (PDB 7E6T)
Data collection and processing		
Magnification	81,000×	81,000×
Voltage (kV)	300	300
Electron exposure (e–/Å^2)	70	70
Defocus range (μm)	–1.5 to –2.5	–1.5 to –2.5
Pixel size (Å)	1.071	1.071
Symmetry imposed	C2	C2
Initial particle images (no.)	2,208,402	1,546,992
Final particle images (no.)	1,215,058	560,366
Map resolution (Å) FSC threshold	6.0 0.143	3.3 0.143
Map resolution range (Å)	3.2–7.0	2.5–6.5
Refinement		
Initial model used (PDB code)	5k5s, 6n51	5k5s, 6n51
Model resolution (Å) FSC threshold	4.3/5.9/8.0 0/0.143/0.5	3.3/3.4/3.7 0/0.143/0.5
Model resolution range (Å)	4.3–8.0	3.3–3.7
Map sharpening *B* factor (Å^2)	–217	–115
Model composition		
Non-hydrogen atoms	14,214	12,751
Protein residues	1796	1592
Ligands	0	PO_4^{3-}: 2
		Ca^{2+}: 6
		NAG: 4
		TNCA: 2
B factors (Å^2)		
Protein	102.59/530.90/286.91	61.44/302.84/157.67
Ligand	N/A	91.52/151.96/105.80
R.m.s. deviations		
Bond lengths (Å)	0.002	0.002
Bond angles (°)	0.559	0.602
Validation		
MolProbity score	2.5	1.49
Clashscore	14	5
Poor rotamers (%)	0	0
Ramachandran plot		
Favored (%)	94	97
Allowed (%)	6	3
Disallowed (%)	0	0

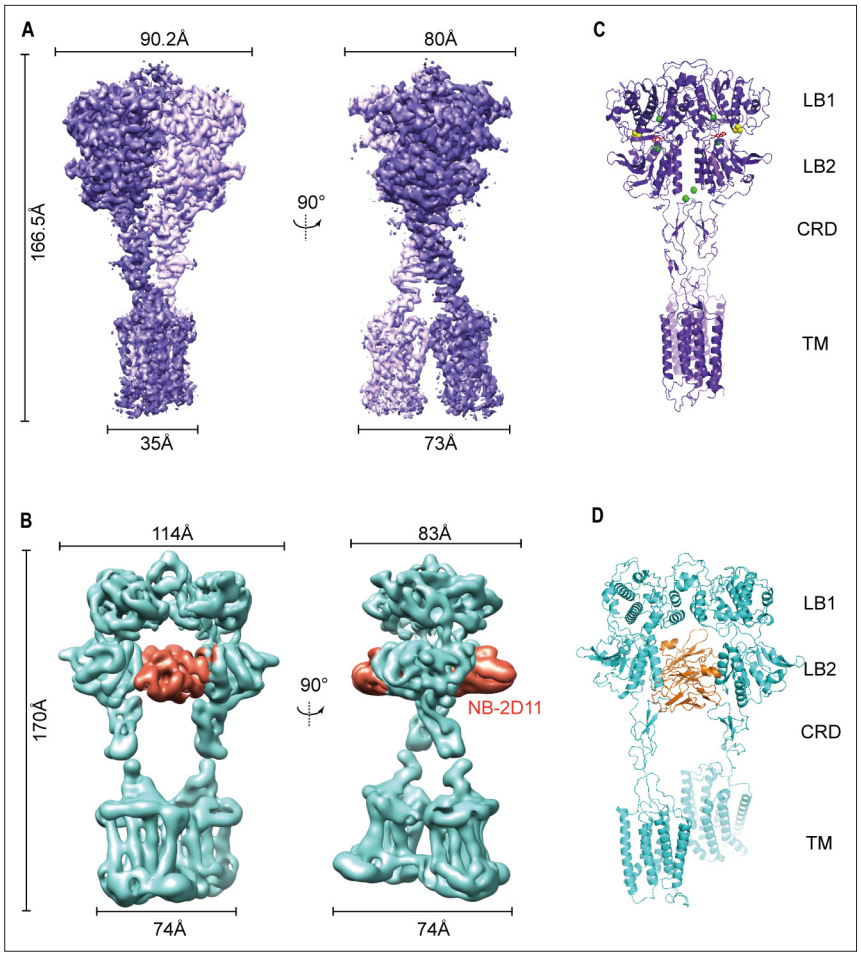

Figure 2. Cryo-EM maps and models of full-length CaSR. (**A**) Left panel shows the view of CaSR in the active conformation (purple) from front view, and the right panel shows the view after a 90° rotation as indicated. (**B**) Left panel shows the view of CaSR in the inactive conformation (cyan) bound to NB-2D11 (orange) from front view, and the right panel shows the view after a 90° rotation as indicated. (**C**) Model (Ribbon representation) of CaSR shows the structure of the active state (purple) bound to TNCA (red) and Ca^{2+} ion (green) viewed from the side. (**D**) Model (Ribbon representation) of CaSR shows the structure of the inactive state (cyan) bind with NB-2D11 (orange).

The online version of this article includes the following figure supplement(s) for figure 2:

Figure supplement 1. Cryo-EM processing workflow of CaSR bound to agonist+PAM.

Figure supplement 2. Agreement between the cryo-EM map of CaSR bound to agonist+PAM and the model.

Figure supplement 3. Cryo-EM maps and models of CaSR.

Figure supplement 4. Cryo-EM processing workflow of inactive CaSR bound to NB-2D11 in GDN.

Figure supplement 5. Comparisons of the structures of CaSR in different conformations.

two totally different VFT module conformations, with their closed–closed conformation presenting similar characteristics to the active state (***Figure 2—figure supplement 5***). This indicates that the CaSR in the inactive state has conformational heterogeneity. In other words, this suggests that in addition to the full inactive state and the active state, there are multiple intermediate states in the process of activation.

Ca^{2+} and TNCA as a composite agonist activate the full-length CaSR dimer

The cryo-EM map of active state presents a distinct density at the ligand-binding cleft of each protomer, which enabled us to unambiguously model TNCA (***Figure 3A,B***). The binding details of TNCA were the same as previously reported data (***Zhang et al., 2016***). The interactions between

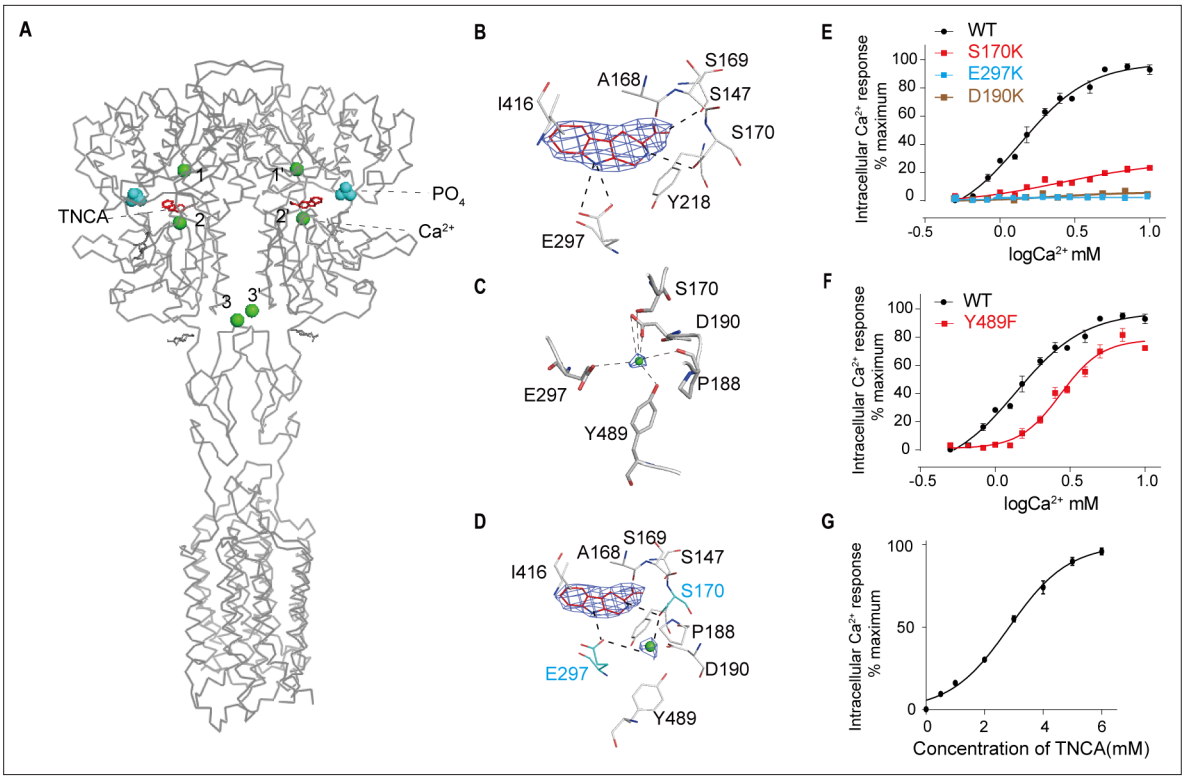

Figure 3. Ca^{2+} and TNCA as a composite agonist activate the full-length CaSR dimer directly. (**A**) Ribbon representation of the active CaSR (gray), showing the location of the Ca^{2+}-binding sites (green sphere) and TNCA (red). (**B**) Specific contacts between CaSR (gray) and TNCA (red space-filling model), mesh represents the final density map contoured at 17σ surrounding. (**C**) Specific interactions between CaSR and newly identified Ca^{2+} ion (green sphere), the mesh represents the cryo-EM density map contoured at 6.0σ surrounding Ca^{2+}. (**D**) Highlighting the newly identified Ca^{2+} and TNCA sharing two common binding residues S170 and E297 (cyan space-filling model). (**E**) Dose-dependent intracellular Ca^{2+} mobilization expressing WT (black dots), mutant S170K (red dots), E297K (cyan dots), and D190K (brown dots) of CaSR. The single mutations were designed based on Ca^{2+} binding sites. N = 4, data represent mean ± SEM (***Figure 3—source data 1***). (**F**) Dose-dependent intracellular Ca^{2+} mobilization expressing WT (black dots), mutant Y489K (red dots) of CaSR. The single mutation was designed based on Ca^{2+} binding sites. N = 4, data represent mean ± SEM (***Figure 3—source data 1***). (**G**) Dose-dependent TNCA-activated intracellular Ca^{2+} mobilization in response to 0.5 mM Ca^{2+} ions. N = 3, data represent mean ± SEM (***Figure 3—source data 2***).

The online version of this article includes the following figure supplement(s) for figure 3:

Source data 1. Intracellular Ca^{2+} flux assay on CaSR mutations.

Source data 2. Intracellular Ca^{2+} flux assay on CaSR-TNCA complex.

Figure supplement 1. Cell surface expression.

TNCA and VFT are primarily mediated by hydrogen bonds (***Figure 3B***). The high-resolution density of active state map enabled us to identify three distinct Ca^{2+}-binding sites within ECD of each protomer (***Figure 3A***). Two sites were previously reported (***Geng et al., 2016***; ***Ling et al., 2021***), while a new Ca^{2+}-binding site was found at the interdomain cleft of the VFT module that is close to the hinge loop and abuts the TNCA binding site, and interacts with both LB1 and LB2 domains to facilitate ECD closure (***Figure 3A–D***). The bound Ca^{2+} ion is primarily coordinated with side chains of D190 and E297, carbonyl oxygen atoms of P188 backbone, and hydroxyl groups of S170 and Y489. Residues P188, D190, and S170 are located in LB1 domain, while E297 and Y489 are in LB2 (***Figure 3C,D***). The main coordination residues (S170, D190, and E297) of the Ca^{2+} ion are consistent with those previously reported (***Liu et al., 2020***). The maps obtained by cryo-EM imaging are insufficient to confirm that the observed density corresponds to calcium. We assume that the density represents the presence of Ca^{2+} based on the following reasons. First, from its hexavalent coordination (coordinating residues P188, D190, S170 and E297, and Y489), this metal is most likely to be Ca^{2+}, although another ion cannot be ruled out. Second, we prepared the CaSR sample in a purification buffer supplemented with 10 mM Ca^{2+} and without any other bivalent cation prior to cryo-EM imaging. Third, the main binding

residues (S170, D190, and E297) of Ca^{2+} ion were previously reported (***Liu et al., 2020***), and that single mutation of these residues (D190K, S170K and E297K, and Y489F) significantly reduced the effect of Ca^{2+}-stimulated intracellular Ca^{2+} mobilization in cells (***Figure 3E***). The cell surface expression levels of these mutants are all above 80 % compared to the wild-type level (***Figure 3—figure supplement 1***). Finally, mutant of a residue that bind L-amino acid (S147A) also largely impaired the Ca^{2+} effect (***Geng et al., 2016***), indicating the presence of L-amino acid near Ca^{2+} ion and that Ca^{2+} activates CaSR through the L-amino acid.

The Ca^{2+} ion interaction with both the LB1 and LB2 domains implies that it also contributes to the closure of the VFT module. The mutation of residue Y489 on LB2 that is in contact with Ca^{2+}, but not L-amino acid, significantly reduces the effect of Ca^{2+}-stimulated intracellular Ca^{2+} mobilization in cells (***Figure 3F***). This indicates that Ca^{2+} on its own is very important for stabilizing the closure of VFT, consistent with findings by ***Liu et al., 2020***. Ling et al. tried to determine the cryo-EM structures of CaSR in the presence of a high concentration of Ca^{2+} to address the question of whether Ca^{2+} ions alone can activate CaSR in the absence of L-Trp. However, they did not obtain the closed conformation of VFT that only contain the Ca^{2+} ion between the cleft. This result indicates that Ca^{2+} ion alone is insufficient to induce the closure of the VFT module even in the presence of a high concentration of Ca^{2+} ions (***Ling et al., 2021***).

Our structure shows that TNCA bind at the interdomain of VFT module (***Figure 3D***, ***Figure 2—figure supplement 2B***), corresponding to the L-amino acid binding site in other class C GPCRs, such as mGluRs and $GABA_B$ receptors. However, it has been reported that Ca^{2+} ion can activate the receptor on its own in various functional assays (***Jensen and Brauner-Osborne, 2007***; ***Liu et al., 2020***; ***Quinn et al., 2004***; ***Saidak et al., 2009***) and L-amino acids enhance the sensitivity of CaSR to Ca^{2+} ion (***Conigrave et al., 2000***; ***Liu et al., 2020***). While L-amino acids and their analogies are generally considered PAMs but not agonists of CaSR, they are the endogenous agonists of other class C GPCRs. This is somewhat inconsistent from the perspective of GPCR classification and evolution.

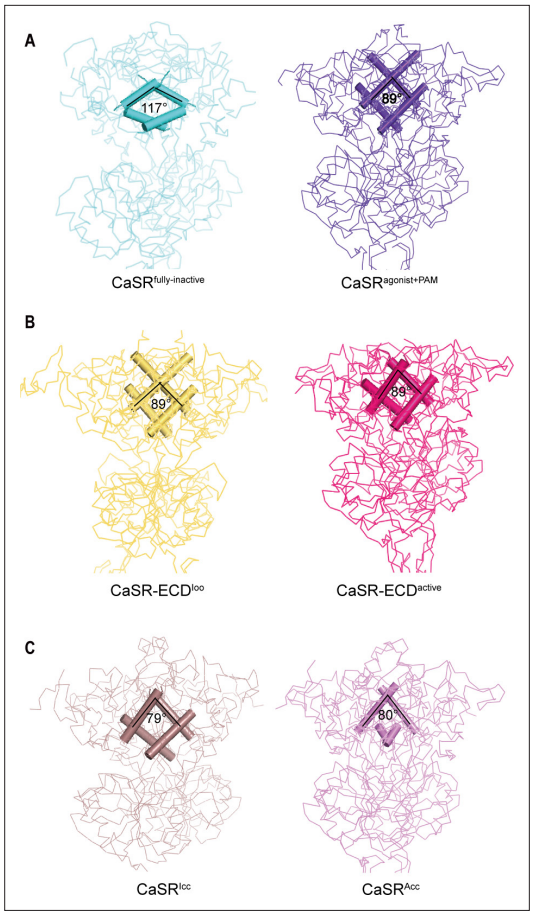

Figure 4. Comparisons of intersubunit LB1 domains interfaces in the inactive and active states of CaSR. (**A**) Left panel: The Cα trace of VFT module of $CaSR^{fully\ inactive}$ cryo-EM structure (cyan). The B-C Helix angle is 117°. Right panel: The Cα trace of VFT module of $CaSR^{agonist+PAM}$ cryo-EM structure (purple). The B-Helix angle is 89°. (**B**) Left panel: The Cα trace of VFT module of crystal structure of CaSR-ECD^{loo} (yellow) (PDB:5K5T). The B-Helix angle is 89°. Right panel: The Cα trace of VFT module of CaSR-ECD^{active} crystal structure (red) (PDB:5K5S). The B-Helix angle is 89°. (**C**) Left panel: The Cα trace of VFT module of $CaSR^{Icc}$ cryo-EM structure (brown) (PDB:7DTW). The B-Helix angle is 79°. Right panel: The Cα trace of VFT module of $CaSR^{Acc}$ cryo-EM structure (lavender) (PDB:7DTV). The B-Helix angle is 80°.

The online version of this article includes the following figure supplement(s) for figure 4:

Figure supplement 1. Comparisons of intersubunit LB1 domains interfaces in the inactive and active states of CaSR.

Our $CaSR^{agonist+PAM}$ structure reveals that the interaction of TNCA with the LB1 and LB2 domains can promote the closure of VFT module, which is a crucial step of the activation for Class C GPCR. The single mutation of the TNCA or L-Trp binding residues (T145I, S147A, S170A, Y218S, E297K) largely impaired the function of the receptor (***Figure 3E***; ***Geng et al., 2016***). This suggests that the TNCA or L-Trp plays an important role during the activation of CaSR. Using intracellular Ca^{2+} flux assays, we

found that TNCA directly activated CaSR in the presence of 0.5 mM of Ca^{2+} ions and that the effect on CaSR was concentration-dependent with EC_{50} of 2.839 mM (***Figure 3G***), in agreement with previous reports that L-Trp directly stimulated intracellular Ca^{2+} mobilization in cells stably expressing CaSR using single-cell intracellular Ca^{2+} microfluorimetry (***Geng et al., 2016***; ***Rey et al., 2005***; ***Young and Rozengurt, 2002***).

It is interesting that our structure shows that the bound Ca^{2+} and TNCA share three common binding residues S170, D190, and E297 (***Figure 3D***). Our experiment has shown that each of single mutations S170A, D190K, and E297K abolishes Ca^{2+}-dependent receptor response (***Figure 3E***), consistent with ***Liu et al., 2020***. Previous studies have suggested that the extracellular Ca^{2+} increases L-Trp binding (***Geng et al., 2016***), and L-Trp also directly stimulates intracellular Ca^{2+} mobilization through CaSR (***Conigrave et al., 2004***; ***Rey et al., 2005***; ***Young and Rozengurt, 2002***) and the efficacy and potency of L-Trp increase with increase in Ca^{2+} concentration (***Geng et al., 2016***). As mentioned above, L-amino acids increase the effect of Ca^{2+} ions on the CaSR (***Jensen and Brauner-Osborne, 2007***; ***Liu et al., 2020***; ***Quinn et al., 2004***; ***Saidak et al., 2009***), and TNCA potentiate the Ca^{2+} activity (***Zhang et al., 2016***). Altogether, we show that CaSR is synergistically activated by the composite agonist composed of TNCA and Ca^{2+} ions.

The conformational transition of the LB1 prepares for the ligand binding during the activation of CaSR

Both inactive and active structures reveal that the interface of LB1–LB1 dimer is predominantly a hydrophobic core, which is formed by the residues on two central helices (B and C) of each protomer, including V115, V149, as well as L156 for inactive structure and L112, L156, L159, and F160 for active crystal structure (***Figure 4A***, ***Figure 4—figure supplement 1A,B***). On the dimer interfaces, The B–C helix angle has rotated approximately 28° from inactive state (117°) to active state (89°) (***Figure 4A***).

Our result is in line with earlier reports of CaSR and other class C GPCRs activation. Liu et al. detected reorientation of LB1–LB1 dimer during activation using a FRET-based conformation CaSR sensor (***Liu et al., 2020***). mGluR5 receptor changes from active to apo state with an approximately 59° rotation of the B–C helix angle (***Koehl et al., 2019***; ***Figure 4—figure supplement 1C,D***).

We then compared the B-C helix angles of previously reported CaSR structures, including CaSR-ECD^{loo}, CaSR-ECD^{active}, $CaSR^{Icc}$, and $CaSR^{Acc}$. No rotation of B–C helix was observed between inactive CaSR-ECD^{loo} and active CaSR-ECD^{active} crystal structures (***Figure 4B***; ***Geng et al., 2016***), despite changing VFT conformation from closed–closed to open–open. Similarly, there was only a small rotation of 1° between $CaSR^{Icc}$ and $CaSR^{Acc}$ (***Figure 4C***; ***Ling et al., 2021***). VFT module of the inactive $CaSR^{Icc}$ adopts a closure conformation, and L-amino acid binds at the interdomain of the VFT (***Ling et al., 2021***); both features are characteristics of an active state. The B–C Helix angle of all four reported structures (CaSR-ECD^{loo}, CaSR-ECD^{active}, $CaSR^{Icc}$, $CaSR^{Acc}$) resemble that of our active $CaSR^{agonist+PAM}$ structure (***Figure 4A–C***).

The B–C helix of the recently reported CaSR structure in the inactive states is same as that of our $CaSR^{agonist+PAM}$, although the 7TMD is similar to that of the inactive state (***Ling et al., 2021***; ***Figure 4C***). The VFT module of the reported $CaSR^{Icc}$ adopts the closure conformation; moreover, the L-amino acid binds at the interdomain of the VFT (***Ling et al., 2021***), which are features of the active state. The rotation of B–C helix is not observed in both the active crystal structures of CaSR ECDs with the closed–closed conformation of VFT module (PDB: 5K5S) and the inactive crystal structure with the open–open conformation of VFT module (PDB: 5K5T), In summary, we propose that these reported conformations should be considered intermediate states in the activation process of CaSR because they exhibit some characteristics of the active state. In our inactive cryo-EM structure, the B–C helix angle is similar to that of mGluRs in the inactive state, with the VFT domain adopting an open–open conformation (***Figure 4A***, ***Figure 4—figure supplement 1C,D***). Therefore, our inactive cryo-EM structure represents the full inactive state. We hereby designate our inactive structure as $CaSR^{fully\ inactive}$.

The LB1 domain plays a predominant role for anchoring ligands. Superimposition of LB1 domains of inactive ($CaSR^{fully\ inactive}$), intermediate (CaSR-ECD^{loo}), and agonist+PAM bound ($CaSR^{agonist+PAM}$) conformations, reveals that our inactive conformation has a significantly different LB1 structure compared to the intermediate conformation (***Figure 4—figure supplement 1E***), whereas the LB1 domains in the intermediate and agonist+PAM bound states are well superimposed with a backbone r.m.s.d. of

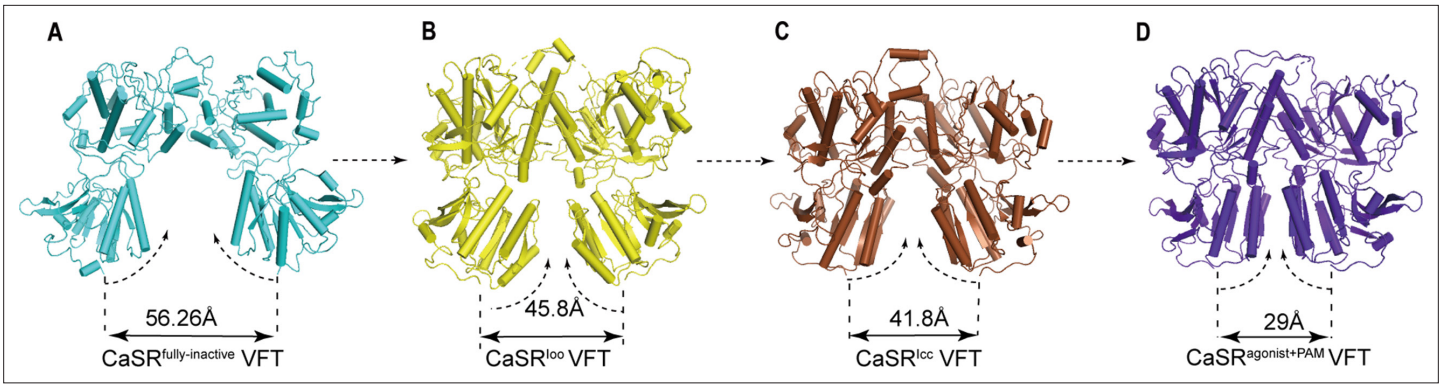

Figure 5. The conformational changes of LB2 domains in three states. (**A**) The CaSR$^{fully\ inactive}$ (cyan) conformation of VFT module. The distance between C termini of the two LB2 domains is 56.26 Å. (**B**) CaSR-ECD^{loo} (yellow) (PDB:5K5T) conformation of VFT module. The distance between C termini of the two LB2 domains is 45.8 Å. (**C**) CaSR^{lcc} (brown) conformation of VFT module (PDB:7DTW). The distance between C termini of the two LB2 domains is 41.8 Å. (**D**) CaSR$^{agonist+PAM}$ (purple) conformation of VFT module. The distance between C termini of the two LB2 domains is 29 Å.

The online version of this article includes the following figure supplement(s) for figure 5:

Figure supplement 1. Superposition of LB1 and VFT domains of CaSR.

0.806 Å (***Figure 4—figure supplement 1F***). Thus, the conformational transition of the LB1 domain from inactive to intermediate state provides the structural basis for ligand binding.

Spontaneous proximity of LB2 domains during the activation

No significant difference of the overall LB2 conformations is observed among the superposition of inactive, intermediate (CaSR-ECD^{loo}), and agonist+PAM bound structures (***Figure 5—figure supplement 1A,B***). The cryo-EM structure of CaSR in inactive state displays a relatively large backbone separation distance of 56.26 Å between the C-terminal ends of N541 of each LB2 domain, while it reduces to 45.8 Å in the CaSR^{loo} state and 41.8 Å in the CaSR^{lcc} state. A further reduction to 29 Å is observed upon activation in the active model (***Figure 5***). Thus, the two LB2 domains gradually approach each other until they interact, a process that is not induced by the agonists (***Figure 5***, ***Figure 5—figure supplement 1C–E***).

NB-2D11 blocks the interaction of LB2 domains to lock the CaSR in the full inactive conformation

The inactive structure reveals that NB-2D11 binds the left lateral of each LB2 domain from orthogonal view (***Figure 6***), with the hydrophilic interaction interface between the amino acids D53, D99, W102, R101, and E110 from CDR1 and CDR3 of the nanobody and the residues R220, S240, S244, Y246, S247, and E251 from Helix F and Strand I (***Figure 6C***). Superposition of the inactive and agonist+PAM bound LB2 domains shows that NB-D211 occupies the spatial position of the LB2 domain of the other protomer, which blocks the approach of another corresponding subunit LB2 (***Figure 6D***). Our results indicate that the interactions of both LB2 domains are required to activate CaSR, which is the explanation of the inhibitory function of NB-2D11.

The rotation of LB2 domain propagates to large-scale transitions of the 7TMDs from TM5-TM6-plane to TM6-driven interface

The closure of VFT displays an inward rotation of each LB2 followed by moving upward individually (***Figure 5***). Afterwards, two intersubunit interfaces are formed at the downstream of subunits, including the interaction between the LB2 linked CRDs, which is consistent with the reported crystal structure of CaSR ECD (***Geng et al., 2016***; ***Figure 7—figure supplement 1***), and the intersubunit interaction between TMDs (***Figure 7A–F***).

The alignment of individual 7TMD of both inactive and agonist+PAM bound states presents that the helices are well superposed (***Figure 7D***). Although NAM and PAM were added during the preparation of inactive and active samples, respectively, no density of them was observed on the maps due to low resolutions. The inactive structure reveals that TM5 and TM6 constitute a 7TMD plane–plane interface

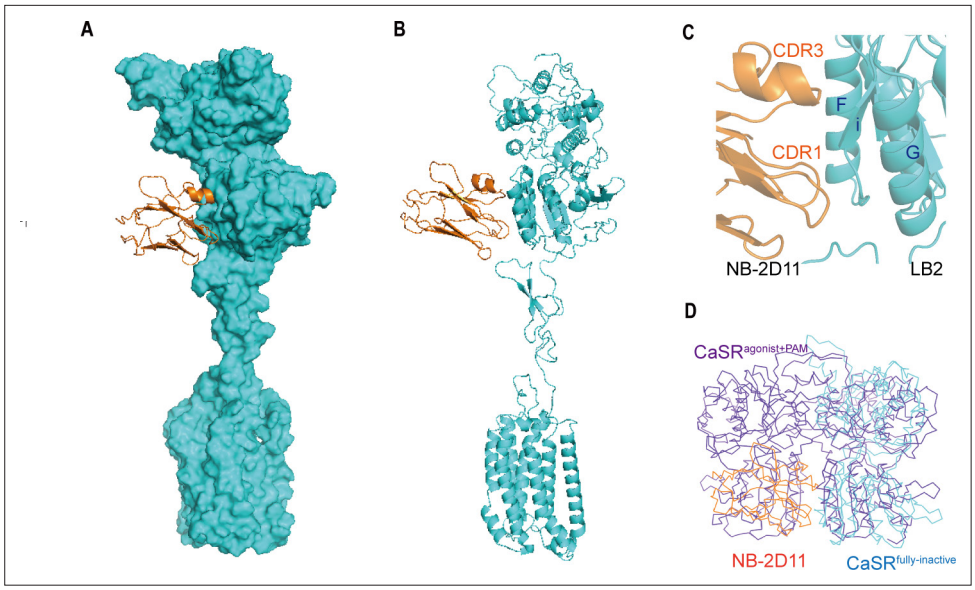

Figure 6. The NB-2D11 blocks the interaction of LB2 domains. (**A**) Structure of the inactive CaSR protomer (surface representation, cyan) with NB-2D11 (ribbon diagram, orange) from front view. (**B**) The NB-2D11 (orange) binds the left lateral of the LB2 (cyan) from the front view of the protomer. (**C**) NB-2D11 binds the LB2 domain through a series of polar interactions through CDR1 and CDR3 of the nanobody and the Helix F and Strand I of the CaSR. (**D**) Superposition of NB-2D11 (orange) binding inactive conformations (cyan) and active (purple) conformations based on the LB2 domain of VFT module, showing the whole NB-2D11 in the inactive state crashes with the LB2 domain of another VFT module in the active state.

(***Figure 7E***). There are pairwise symmetrical undefined maps that link the extracellular and intracellular part of TM5 and TM6 in the 7TMD interface (***Figure 7—figure supplement 2A***). Our structure shows a TM5–TM6/TM5–TM6 interaction that it is slightly different from the TM4–TM5/TM4–TM5 plane–plane interaction in the 7TMD interface proposed by ***Liu et al., 2020***. Our experiments show that each of the single mutations F789A or F792A attenuates Ca^{2+}-induced receptor activity, indicating that this contact plays a role in the activation of CaSR (***Figure 7H,I***). The cell surface expression levels of these mutants are all over 100 % compared to the wild-type level (***Figure 3—figure supplement 1***).

The agonist+PAM bound structure shows a TM6–TM6 interface, contacting at the apex of TM6 helices, which is a hallmark of GPCR activation (***Koehl et al., 2019***; ***Figure 7B,F***). To further validate the role of this interface, mutation to P823 in TM6 markedly reduced Ca^{2+}-induced receptor activity (***Figure 7J***), indicating that the TM6–TM6 interface is crucial to CaSR activation, consistent with previous studies. Liu et al. reported an interface mediated by TM6 in their active CaSR structure and showed that a cysteine cross-linking at residue $A824^{6.56}$ in TM6 led to a constitutively active receptor (***Liu et al., 2020***). Similarly, active mGluR5 (***Koehl et al., 2019***) and $GABA_B$ receptors (***Kim et al., 2020***; ***Mao et al., 2020***; ***Papasergi-Scott et al., 2020***; ***Shaye et al., 2020***) have the same TM6–TM6 interface (***Figure 7F***; ***Figure 7—figure supplement 2B,C***). TM6 cross-linked mGluR5 and TM6-locked mGluR2 were activated continuously (***Koehl et al., 2019***; ***Xue et al., 2015***).

Superposition of inactive and agonist+PAM structures shows a high degree of structural overlap in 7TM domains, with the exception of a bundle comprising of extracellular loop 2 (ECL2) and a stalk linking CRD and TM1 showing slight structural dissimilarity. CRD appears semi-rigid (***Figure 7C***). Therefore, a small rotation of LB2 domains could propagate to large-scale transitions of the TMDs through the CRDs, thereby reorientating the 7TMDs from the inactive plane–plane interface mediated by TM5 and TM6 to the active interface driven by TM6 (***Figure 7E–G***). The proximity of 7TMDs is observed during the activation, from a plane–plane distance of 24 Å in inactive state to 5.7 Å at $P823^{6.55}$ in the active state (***Figure 2—figure supplement 3A,B***).

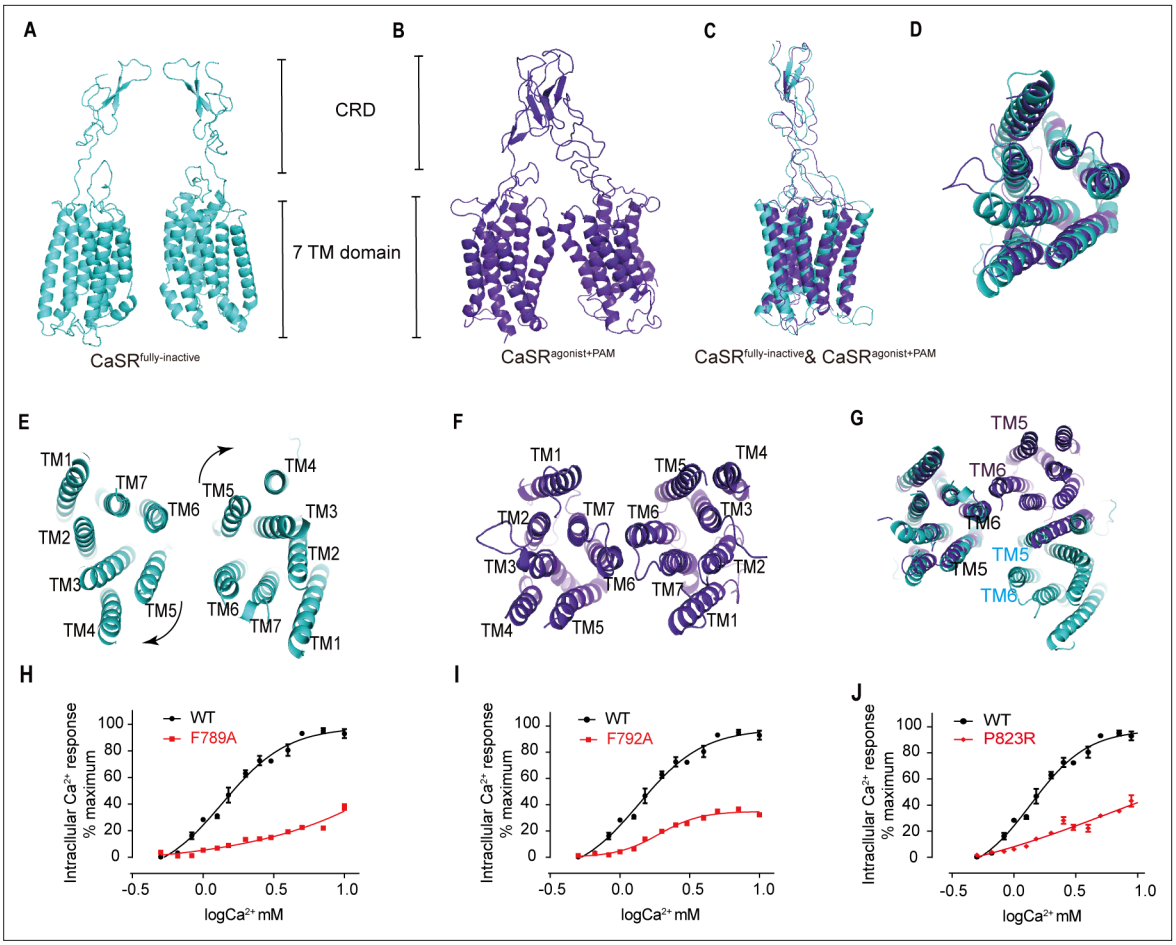

Figure 7. The closure of VFT leading to the rearrangement of inter-7TMDs. (**A**) Front view of CaSR$^{fully\ inactive}$ CRDs and 7TMDs (cyan). (**B**) Front view of CaSR$^{agonist+PAM}$ CRDs and 7TMDs (purple). (**C**) The alignment of the part of CRD and 7TMDs in both fully inactive and agonist+PAM bound CaSR. (**D**) The alignment of inactive and agonist+PAM bound 7TMDs from top view. (**E–G**) The 7TMDs interface in the fully inactive state of CaSR is mediated by TM5 and TM6 (cyan) from top view and that of the agonist+PAM state is driven by TM6 from top view. Superposition of 7TMD of the inactive (cyan) and agonist+PAM bound CaSR (purple) show the rotation of 7TMDs. (**H–J**) Dose-dependent intracellular Ca^{2+} mobilization expressing WT (black dots) and mutant (red dots) CaSR (***Figure 7—source data 1***). The single mutations of F789A (**H**), F792A (**I**), and P823R (**J**) were designed based on the inactive density map. For (**H–J**), N = 4, data represent mean ± SEM.

The online version of this article includes the following figure supplement(s) for figure 7:

Source data 1. Intracellular Ca^{2+} flux assay on various CaSR mutations.

Figure supplement 1. The homodimer interface of the CRDs in the active state of CaSR.

Figure supplement 2. Conformational change of the 7TMDs interface during activation.

Upward movement of LB2 converted into the intra-7TM rearrangement through ECL2

Models of both inactive and active structures reveal that there is a bundle of structure in the junction region between extracellular and transmembrane domain, which is composed of C-terminal elongated peptide of CRD and the twisted hairpin loop of ECL2 (***Figure 8A,B***). Unlike mGluR5 and $GABA_B$ receptors (***Kim et al., 2020***; ***Koehl et al., 2019***; ***Mao et al., 2020***; ***Papasergi-Scott et al., 2020***; ***Park et al., 2020***; ***Shaye et al., 2020***), which are formed by a twisted three-strand β-sheet, the junction of CaSR is more flexible than that of mGluR5 and $GABA_B$ receptors. The structure of the agonist+PAM bound state shows that the residues 759–763 fragment of ECL2 and the C-terminal residues of the CRD (601–604) form a new interface (***Figure 8A***), which presents a more compactible interaction in the agonist+PAM bound state (***Figure 8B***). In addition, there is another interface involving the residues E759 at the apical loop of ECL2 and the residues W590 at the bottom of the loop composed of

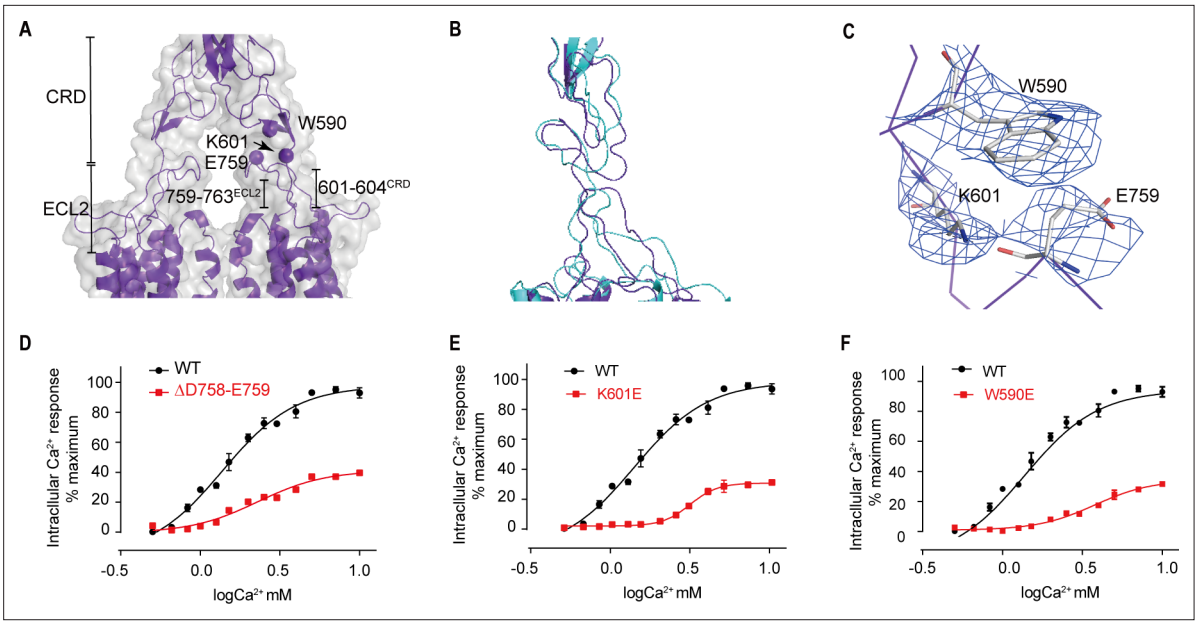

Figure 8. Upward movement of LB2 is converted into the intra-7TM conformational rearrangement through ECL2. (**A**) Model in $CaSR^{agonist+PAM}$ state (purple) and cryo-EM map (gray) showing the contact between the CRD and the ECL2 of the 7TMDs. Critical residues at this interface are shown as spheres at their Cα positions. (**B**) Superposition of the interface between the CRD and the ECL2 of the 7TMD between both fully inactive and agonist+PAM bound conformations. (**C**) Specific contacts between the loop of CR domain and the loop of ECL2 to shift the ECL2 up. (**D–F**) Deletion of residues D758 and E759 (**D**), the single mutation of K601E (**E**) and W590E (**F**) significantly reduced Ca^{2+}-induced receptor activity. (WT in black dots and mutant in red dots). For (**D–F**), N = 4, data represent mean ± SEM (***Figure 8—source data 1***).

The online version of this article includes the following figure supplement(s) for figure 8:

Source data 1. Intracellular Ca^{2+} flux assay on CaSR mutations.

residues 589–591 for agonist+PAM bound state. In the agonist+PAM bound state, the loop of ECL2 is pulled up by the interaction among E759, W590, and K601, leading to the movement of ECL2 (***Figure 8***), which would raise the reorientation of TM5 and TM6 domains during the activation of CaSR (***Figure 7E,F***). To confirm the importance of this interaction, deletion of residues D758 and E759 at the apex of ECL2 (***Figure 8D***), as well as single mutations of K601E and W590E (***Figure 8E,F***), disrupted these contacts and led to a significantly reduced Ca^{2+}-induced receptor activity, Therefore, ECL2 plays a key role in relaying the conformational changes of VFT to the intrasubunit TM domain to rearrange the structure to adapt to downstream transducers, such as G proteins. The cell surface expression levels of Δ758–759 mutant was comparable to that of WT, while W590E and K601E mutants were expressed on the cell surface at approximately 40–50% of WT level (***Figure 3—figure supplement 1***).

Discussion

In this study, we have determined the cryo-EM structures of CaSR in the fully inactive and agonist+PAM bound states. During the preparation of our manuscript, several CaSR structures have been reported, including structures of closed–closed conformation in the inactive state ($CaSR^{Icc}$ and $CaSR^{Trp}$) and closed–closed conformation of Ca^{2+}/Trp bound state ($CaSR^{Acc}$ and $CaSR^{Ca}$). Open-closed and open–open conformations ($CaSR^{Ioc}$ and $CaSR^{Ioo}$) have also been observed; however, they were not built due to low resolution (***Ling et al., 2021***). The overall conformation of our $CaSR^{agonist+PAM}$ structure is almost identical to that of $CaSR^{Acc}$, while the open–open conformational VFT module in our inactive structure ($CaSR^{fully\ inactive}$) is different from the closed–closed conformation in their reported inactive $CaSR^{Icc}$ structures. In addition, the main conformation changes of CaSR during activation were also described (***Liu et al., 2020***). Complemented with solved crystal structures of CaSR ECD and full-length cryo-EM structures of other class C GPCR, these recent findings allow us to understand the structural framework and essential events that occur during the activation of CaSR. The overall structures of CaSR resemble the recently published structures of mGluR5

and $GABA_B$ receptors, indicating that the structural mechanism of class C GPCRs is similar (***Kim et al., 2020***; ***Koehl et al., 2019***; ***Mao et al., 2020***; ***Papasergi-Scott et al., 2020***; ***Park et al., 2020***; ***Shaye et al., 2020***).

Multiple structural and functional studies of class C GPCR have demonstrated that there are two typical conformational changes in the VFT domains during receptor activation. One is that the B–C helix angle at the interfaces of LB1–LB1 dimer sharply rotated from inactive to active state. This conformational transition of the LB1 domain is conducive to ligand binding, which is a prerequisite for receptor activation (***Figure 5—figure supplement 1A,B***). For example, increased glutamate affinity and occupancy in mGluR2 active conformation were observed by the mutations in B-Helix (***Levitz et al., 2016***). Another is that the conformation of VFT domain is converted from open to closed for the change of interdomain in one protomer, which is a landmark event during receptor activation.

We used an inhibitory nanobody to stabilize the conformation of CaSR in the inactive state. Our inactive structure shows that the B-C helix angle is about 117° and VFT domain adopts an open–open conformation (***Figure 4A***). The B–C helix angle has rotated approximately 28° from inactive to agonist+PAM bound state and the VFT domain rearranged from open–open configuration to closed–closed configuration during CaSR activation (***Figures 4A and 5***), consistent with other class C GPCR activation mechanism findings. In addition, Liu et al. developed a FRET-based conformation sensor for CaSR through fusion of SNAP-tag at its N-terminus of CaSR subunit to label with fluorophores. Their data showed that the CaSR dimer underwent a large conformational change of LB1–LB1 dimer during activation, in which the B–C helix angle rotated from inactive to active state as the fluorophores labeled the N-terminus of LB1 domain (***Liu et al., 2020***). We used nanobody NB-2D11 to block the proximity of LB2 domains, thus locking the CaSR in an inactivate state (***Figure 6***). Altogether, our structural and functional assay data suggest that our inactive cryo-EM structure represents the full inactive state of CaSR.

The rotation of LB1–LB1 domains is a watershed between inactive and intermediate states. We have reported that the crystal structure of CaSR-ECD in the open-open state ($CaSR^{loo}$) has the same B–C helix angle as that of the active state ($CaSR^{agonist+PAM}$), with LB1 domain configuration that is ready for L-amino acid and Ca^{2+} binding, in contrast to our cryo-EM structures of the inactive state (***Figure 5—figure supplement 1A,B***). Similarly, the recently reported conformation $CaSR^{lcc}$ has the similar B–C helix angle as $CaSR^{agonist+PAM}$, but adopts the closed–closed VFT conformation, which is a feature of the active state. It is likely that both CaSR-ECD^{loo} and $CaSR^{lcc}$ are different intermediate states during the activation of CaSR. We believe that the inhibition with NB-2D11 pushes the CaSR to a completely inactive state.

At present, the prevailing view is that the principal agonist of CaSR is extracellular Ca^{2+} (***Hofer and Brown, 2003***). L-amino acids, such as L-Trp, can enhance the sensitivity of CaSR toward Ca^{2+} ions (***Conigrave et al., 2000***), and are considered as PAMs of the receptor (***Saidak et al., 2009***). In line with this view, a recently reported FRET study showed that Ca^{2+} ions are sufficient to activate CaSR in the absence of L-amino acids, such that Ca^{2+} could be considered as an agonist of CaSR, whereas L-amino acids are pure PAMs of CaSR (***Liu et al., 2020***). However, it is interesting to note that L-amino acids or their analogs are endogenous agonists of other class C GPCRs, suggesting inconsistency from the perspective of GPCR classification and evolution.

In contrast, some studies have also shown that if Ca^{2+} concentration is higher than the threshold of 0.5 mM, L-amino acid can activate the receptor (***Conigrave et al., 2004***; ***Conigrave et al., 2000***; ***Rey et al., 2005***; ***Young and Rozengurt, 2002***), indicating that Ca^{2+} and L-amino acid can act as co-agonists of the receptor. Using single-cell intracellular Ca^{2+} microfluorimetry, L-Trp has been shown to directly stimulate intracellular Ca^{2+} mobilization in cells stably expressing CaSR, with its efficacy and potency increase with increases in concentration of Ca^{2+} ions, hence providing direct evidence that L-amino acids are agonists of CaSR (***Geng et al., 2016***). However, this view has yet to be widely accepted because it is difficult to observe L-amino acids directly activating CaSR. The mode of action of Ca^{2+} ion and L-amino acids on CaSR remains controversial.

Our $CaSR^{agonist+PAM}$ structure shows that TNCA and a newly identified Ca^{2+} ion bind at the inter-domain cleft of the VFT module, and they both interact with both LB1 and LB2 domains to facilitate ECD closure (***Figure 3A***), therefore forming the closed state of the ligand-binding domain required for CaSR activation. This indicates that both TNCA and the Ca^{2+} ion contribute to the activation of CaSR. TNCA and the bound Ca^{2+} share three common binding residues S170 and D190 of LB1 domain

and E297 from LB2 domain (***Figure 3E,F***), which suggest that the CaSR is synergistically activated by TNCA and Ca^{2+} ions.

Our experiments have shown that TNCA directly stimulate intracellular Ca^{2+} mobilization in cells stably expressing CaSR (***Figure 3G***), suggesting that TNCA are agonists of CaSR. The structure of CaSR shows that TNCA binds at the cleft between LB1 and LB2 domains, which is the binding site for all class C GPCR agonists (***Geng et al., 2013***; ***Geng et al., 2016***; ***Kunishima et al., 2000***; ***Muto et al., 2007***; ***Tsuchiya et al., 2002***), and TNCA has a binding pattern similar to that of the endogenous agonists of mGluR and $GABA_B$ receptors (***Figure 3D***; ***Geng et al., 2016***). The key coordination residues are very conserved, such as S147 and S170 (***Geng et al., 2013***; ***Geng et al., 2016***; ***Kunishima et al., 2000***; ***Zhang et al., 2016***). Moreover, TNCA (or L-Trp) interact with residues from LB1 and LB2 to stabilize the closure of VFT, and the signal mutation of the contacting residues (T145I, S147A, S170A, Y218S, E297K) substantially reduce the function of the receptor, even if some of these residues (S147A, T145I, and Y218S) are not related to the coordinating residues of Ca^{2+}, hence indicating that TNCA or L-Trp plays a key role in the activation of CaSR (***Geng et al., 2016***).

In addition, Ling et al. tried to determine the cryo-EM structures of CaSR in the presence of a high concentration of Ca^{2+} to address the question of whether Ca^{2+} ions alone can activate CaSR in the absence of L-Trp. Three different 3D models were obtained, in which the VFT adopted closed–closed, closed–open, and open–open conformations, and an undefined L-amino acid or its derivate was buried in the closed VFT module. However, they did not obtain the closed conformation of VFT containing only Ca^{2+} ion between the cleft (***Ling et al., 2021***). The results indicate that Ca^{2+} ion alone is not enough to induce the closure of the VFT module even in the presence of a high concentration of Ca^{2+} ion, and L-amino acid or its derivate is required to stabilize the closed conformation of VFT module. Altogether, L-amino acids are the endogenous agonists of CaSR, in agreement with that of other class C GPCRs.

It remains controversial whether Ca^{2+} act alone to activate CaSR in the absence of L-amino acid. Three different groups prepared CaSR samples without L-amino acids or derivatives for crystal or cryo-EM structural studies, but they all unexpectedly obtained the active structure of CaSR or CaSR ECD with closed–closed VFT conformation containing undefined ligands (***Geng et al., 2016***; ***Ling et al., 2021***; ***Zhang et al., 2016***). This ligand was subsequently identified as TNCA, which had a high affinity for CaSR, and potentiated Ca^{2+} activity (***Zhang et al., 2016***). As we all know, it takes a long time to purify CaSR in TNCA-free buffer for structural study; nevertheless, the endogenous TNCA would still bind to CaSR. This indicates that TNCA tightly binds to CaSR or that it is buried in closed VFT module such that it is difficult to be washed off.

Gentle washing is impossible to remove TNCA bound to CaSR in various function assays. In the absence of TNCA (or L-amino acid) and despite well-controlled assays, it is possible that endogenous TNCA would still bind to CaSR to stabilize the closed conformation of VFT. It would then appear that Ca^{2+} ions directly activate the CaSR alone as TNCA remains undetected.

In addition to the role of Ca^{2+} ion binding at the cleft of VFT module to stabilize the closed conformation of VFT, another role of the Ca^{2+} ions should be considered, in which Ca^{2+} ion is coordinated by D234, E231, and G557, and bridges the LB2 domain of one subunit and the CR domain of the second subunit. Ca^{2+} ion facilitates the formation of the active conformation of CaSR, which explain why L-amino acids (or TNCA) can activate CaSR in the presence of Ca^{2+} ion above the threshold concentration of 0.5 mM. We speculate that as endogenous TNCA exists, binds to CaSR with high affinity, and is difficult to be replaced by other added L-amino acids, it is challenging to observe whether L-amino acids can directly activate CaSR. Alternatively, the observed allosteric regulation is also a comprehensive result when we performed function assay. It needs the experience of the kinetics and dynamics of L-amino acid or TNCA binding with CaSR to confirm.

We observed that the LB2 domains approach each other during CaSR activation. Although we do not have a fully active conformation of the CaSR without agonist binding as evidence, crystal structures of a fully closed VFT modules of mGluR1 with or without agonist binding were previously reported (***Kunishima et al., 2000***) and have demonstrated that the proximity of both LB2 domains is an automatic process rather than an agonist-driven one. Here, we showed that NB-2D11 inhibited CaSR activation by blocking the proximity of both LB2 domains.

We analyzed how the closure of ligand bound VFT module is relayed to the signaling of 7TMDs through the CRDs. First, the rotation of LB2 domain is propagated to the large-scale transition of

intersubunit 7TMDs, which leads to rearrangement of 7TMDs interface from TM5–TM6-plane/TM5–TM6-plane interface to TM6–TM6-mediated interface. Liu et al. used FRET sensor to investigate the 7TM interface rearrangement during the activation of the CaSR through a disulfide cross-linking approach. They observed a TM4–TM5-plane/TM4–TM5-plane interface in the inactive state, but a TM6–TM6 contact in the active state of the CaSR dimer (***Liu et al., 2020***). The conformational heterogeneity of the interface of 7TMDs in the inactive state indicates that there is a possible dynamic equilibrium between the TM4–TM5 and TM5–TM6 interfaces. TM6–TM6 contact in the active state is considered to be a hallmark of class C GPCR activation. For mGluR5 and $GABA_B$ receptors, the 7TMDs rearrange from TM5–TM5 interface in the inactive state to TM6–TM6 interface in the active state (***Kim et al., 2020***; ***Koehl et al., 2019***; ***Mao et al., 2020***; ***Papasergi-Scott et al., 2020***; ***Park et al., 2020***; ***Shaye et al., 2020***). In addition, structures of $GABA_B$ receptor revealed some cholesterol molecules at the interface of 7TMDs (***Kim et al., 2020***; ***Mao et al., 2020***; ***Papasergi-Scott et al., 2020***; ***Park et al., 2020***; ***Shaye et al., 2020***). It is possible that the undefined maps between the 7TMD in our full inactive structure could be sterols that separate the dimer plane–plane interface and stabilize the inactive state (***Figure 7—figure supplement 2A***). In this study, we found that the conformation of ECL2 changed from the inactive to agonist+PAM state. However, the alignment of individual 7TM of both inactive and agonist+PAM states shows that the helices are well superposed, indicating that the change of ECL2 conformation is unable to drive the rearrangements of TM4 and TM5 helices and stabilize the active conformation in the TMDs (***Koehl et al., 2019***) This observation is consistent with findings that the active state of mGluR5 is stabilized by G proteins (***Koehl et al., 2019***; ***Manglik et al., 2015***; ***Rosenbaum et al., 2011***). It is required to determine the structure of G protein coupling CaSR to clarify the configuration of the 7TMD in the active state.

Materials and methods

Key resources table

Reagent type (species) or resource	Designation	Source or reference	Identifiers	Additional information
Gene (*Homo sapiens*)	CaSR	NCBI	NM_000388.4	
Strain, strain background (*Escherichia coli*)	BL21(DE3)	New England Biolabs	Cat#: C2527I	*E. coli* strain for expression of the nanobody
Strain, strain background (*Escherichia coli*)	TG1	Lucigen	Cat#: 60,502	Electrocompetent cells
Strain, strain background (*Escherichia coli*)	TOP10F'	Huayueyang Biotech	WXR15-100S	*E. coli* strain for expression of the nanobody
Cell line (*Homo sapiens*)	(HEK) 293 S GnTI$^-$ cells	ATCC	Cat# CRL-3022 RRID: CVCL_A785	Mycoplasma negative
Cell line (*Homo sapiens*)	HEK 293T/17	ATCC	Cat# CRL-11268 RRID: CVCL_1926	Mycoplasma negative
Antibody	HA-Tag, (Mouse monoclonal)	Yeasen	30,701ES60	Dilution: (1/2000)
Antibody	Flag-Tag (DYKDDDDK), (Mouse monoclonal)	Yeasen	30,503ES20	Dilution: (1/2000)
antibody	Peroxidase AffiniPure Goat Anti-Mouse IgG (H + L) (Goat monoclonal)	Yeasen	33,201ES60	Dilution: (1/2500)
Recombinant DNA reagent	AxyPrep Plasmid Miniprep Kit	CORNING LIFE SCIENCES	Cat#:220	
Recombinant DNA reagent	pMECS vector	BioVector NTCC	pMECS	Phage display vector
Recombinant DNA reagent	pEG BacMam vector	Addgene	Cat#:160,451	Vector
Recombinant DNA reagent	pCMV-HA	Addgene	Cat#:631,604	Vector

Continued on next page

Continued

Reagent type (species) or resource	Designation	Source or reference	Identifiers	Additional information
Recombinant DNA reagent	pcDNA3.1	Addgene	Cat#:128,034	Vector
Peptide, recombinant protein	Flag peptide	Genscript		DYKDDDDK
Peptide, recombinant protein	NB88 (camel nanobody)	This study		Isolated from phage display library of immunized cammel with hCaSR
Peptide, recombinant protein	NB-2D11 (camel nanobody)	This study		Isolated from phage display library of immunized cammel with hCaSR
Commercial assay or kit	Luciferase assay kit	Promega	E152A	For signaling assay
Commercial assay or kit	SuperSignal ELISA Femto Substrate	Thermo Scientific	Cat#: 37,075	Protein Assays and Analysis
Commercial assay or kit	Fluo-4, AM, Cell Permeant	YEASEN	40,704ES50	
Chemical compound, drug	TNCA	aladdin	42438-90-4	
Chemical compound, drug	NPS-2143	aladdin	284035-33-2	
Chemical compound, drug	cinacalcet	aladdin	364782-34-3	
Chemical compound, drug	Lauryl Maltose Neopentyl Glycol (LMNG)	Anatrace	NG310	Membrane protein purification
Chemical compound, drug	Glyco-Diosgenin (GDN)	Anatrace	GDN101	Membrane protein purification
Chemical compound, drug	Cholesterol Hemisuccinate tris Salt (CHS)	Anatrace	CH210	Membrane protein purification
Chemical compound, drug	TMB substrate	Thermo Fisher Scientific	34,021	Protein Assays and Analysis
Software, algorithm	cryoSPARC	https://cryosparc.com	Version 3.0.0 RRID:SCR_016501	Cryo-EM data processing
Software, algorithm	PHENIX	http://www.phenix-online.org/	Version 1.19.2 RRID:SCR_014224	Structure refinement
Software, algorithm	Coot	Coot (cam.ac.uk)	Version 0.9.4 RRID:SCR_014222	Structure refinement
Software, algorithm	MolProbity	DOI:10.1107/S0907444909042073	RRID:SCR_014226	Structure verification
Software, algorithm	UCSF Chimera	https://wwwcgl.ucsf.edu/chimera/ (PMID:15264254)	Version 1.15 RRID:SCR_004097	Initial homology model docking
Software, algorithm	PyMol	Schrodinger	Version 2.5 RRID:SCR_000305	Structural visualization/figure preparation
Software, algorithm	GraphPad Prism 7	GraphPad	RRID:SCR_002798	Analysis of signaling data
Other	Lipofectamine 2000	Invitrogen	11668030	Transfection reagent for signaling assay

Cell lines

(HEK) 293 S GnTI$^-$ cells (human) were purchased from ATCC (Cat# CRL-3022 RRID:CVCL_A785), which were grown in FreeStyle 293 medium (Gibco) supplemented with 2 % (v/v) FBS (Gibco) and 8 % CO_2 for maintenance. HEK293T/17 cells (ATCC, Cat# CRL-11268 RRID:CVCL_1926) were grown in Dulbecco's modified eagle medium (DMEM, Gibco) supplemented with 10 % (v/v) FBS and 5 % CO_2. All cell lines were grown at 37°C. All the cell lines tested negative for mycoplasma contamination.

Nanobody library generation

Camel immunizations and nanobody library generation were performed as described previously (***Pardon et al., 2014***). Animal work was conducted under the supervision of Shanghai Institute of

Materia Medica, Chinese Academy of Sciences. In brief, two camels were immunized subcutaneously with approximately 1 mg human CaSR protein combined with equal volume of Gerbu FAMA adjuvant once a week for seven consecutive weeks. Three days after the last immunization, peripheral blood lymphocytes (PBLs) were isolated from the whole blood using Ficoll-Paque Plus according to manufacturer's instructions. Total RNA from the PBLs was extracted and reverse transcribed into cDNA using a Super-Script III FIRST-Strand SUPERMIX Kit (Invitrogen). The VHH encoding sequences were amplified with two-step enriched-nested PCR using VHH-specific primers and cloned between *PstI* and *BstEII* sites of pMECS vector. Electro-competent *E. coli* TG1 cells (Lucigen) were transformed and the size of the constructed nanobody library was evaluated by counting the number of bacterial colonies. Colonies were harvested and stored at −80 °C.

Nanobody identification by phage display

E. coli TG1 cells containing the VHH library were superinfected with M13KO7 helper phages to obtain a library of VHH-presenting phages. Phages presenting CaSR-specific VHHs were enriched after three rounds of biopanning. For each panning round, phages were dispensed into CaSR coated 96 wells (F96 Maxisorp, Nunc), incubated for 2 hr on a vibrating platform (700 r.p.m), and subsequently washed 10 times with PBST and five times with PBS. The retained phages were eluted with 0.25 mg ml^{-1} trypsin (Sigma-Aldrich). The collected phages were subsequently amplified in *E. coli* TG1 cell for consecutive rounds of panning. After the third rounds of biopanning, 200 positive clones were picked and infected with M13KO7 helper phages to obtain the VHH-presenting phages.

ELISA to select CaSR VHHs

The wells of ELISA plates were coated with 2 μg ml^{-1} neutravidin in PBS overnight at 4 °C. Biotinylated CaSR (2 μg ml^{-1}) was added into each well. Then the wells were blocked with 5 mg ml^{-1} non-fat milk powder in PBS. One hundred microliter supernatant of HA-tagged CaSR VHH was added into each well with 1 hr incubation at 4 °C, followed by incubation with horseradish peroxidase (HRP)-conjugated anti-HA (Yeasen). TMB substrate (Thermo Fisher Scientific) was added, and the reactions were stopped by 2 M H_2SO_4. Measurement was performed at 450 nm.

Purification of NB-2D11

NB-2D11 was cloned into a pMECS vector (NTCC) that contains a PelB signal peptide and a hemagglutinin (HA) tag followed by a 6× histidine tag at the C-terminus. It was expressed in the periplasm of *E. coli* strain TOP10F' (Huayueyang Biotech) and grown to a density of OD_{600nm} 0.6–0.8 at 37 °C in 2YT media containing 100 μg/ml Ampicillin, 0.1 % (w/v) glucose and 1 mM $MgCl_2$, and then induced with 1 mM IPTG at 28 °C for 12 hr. The bacteria were harvested by centrifugation and resuspended in a buffer containing 20 mM HEPES pH 7.5, 150 mM NaCl, 1 mM PMSF, and lysed by sonication, then centrifuged at 4000 r.p.m. to remove cell debris. The supernatant was loaded onto Ni-NTA resin and further eluted in elution buffer containing 20 mM HEPES pH 7.5, 150 mM NaCl, and 300 mM imidazole. The elution was purified by gel filtration chromatography using a HiLoad 16/600 Superdex 75 pg column in 150 mM NaCl with 20 mM HEPES pH7.5. Finally, NB-2D11 was flash-frozen in liquid nitrogen until further use.

Purification of inactive state CaSR bound to NPS-2143 and NB-2D11

Human CaSR (1-870) followed by a Flag epitope tag (DYKDDDD) at the C-terminus was cloned into a modified pEG BacMam vector (***Goehring et al., 2014***) for expression in baculovirus-infected mammalian cells. Human embryonic kidney (HEK) 293 $GnTI^-$ cells (ATCC) were infected with baculovirus at a density of 2.5 × 10^6 cells per ml at 37 °C in 8 % CO_2. Ten millimolar sodium butyrate was added 12–16 hr postinfection, then cells were grown for 48 hr at 30 °C with gentle rotation.

The infected cells were harvested by centrifugation at 4000 g for 30 min, resuspended, and homogenized using a dounce tissue grinder (WHEATON) in hypotonic buffer (20 mM HEPES pH7.5, 10 mM NaCl, 1 mM $CaCl_2$, 10 % glycerol, 1× cocktail of protease inhibitor, and 1 μM NPS-2143). Cell membrane was collected by ultra-centrifugation at 40,000 r.p.m. in a Ti-45 rotor (Beckman Coulter) for 1 hr. Then the membrane was resuspended and solubilized in buffer containing 20 mM HEPES, 150 mM NaCl, 1 mM $CaCl_2$, 10 % glycerol, 1 μM NPS-2143, 1 % (w/v) lauryl maltose neopentyl glycol (LMNG) (Anatrace), and 0.1 % (w/v) cholesteryl hemisuccinate TRIS salt (CHS) (Anatrace) for 1 hr at

4 °C with constant stirring. The supernatant was collected by ultra-centrifugation at 40,000 r.p.m. for 1 hr and applied to an anti-Flag M2 antibody affinity column (Sigma-Aldrich). After receptor binding to the M2 column, the resin was washed with 20 mM HEPES, 150 mM NaCl, 1 mM $CaCl_2$, 10 % glycerol, 1 μM NPS-2143, 0.1 % LMNG, 0.01 % CHS. The column was washed stepwise with decreasing proportion of LMNG and increasing concentration of GDN/CHS to 0.2%/0.02 %. CaSR was then eluted with 20 mM HEPES, 150 mM NaCl, 1 mM $CaCl_2$, 10 % glycerol, 1 μM NPS-2143, 0.02 % GDN, 0.002 % CHS, and 0.2 mg ml^{-1} Flag peptide.

CaSR was further purified by ion-exchange chromatography using a Mono Q 5/50 GL column. Peak fractions were assembled and incubated with a 1.2 molar excess of NB-2D11 for 1 hr before injection on a Superose 6 Increase 10/300 GL column. Fractions of CaSR-NB-2D11 complex in buffer containing 20 mM HEPES, 150 mM NaCl, 1 mM $CaCl_2$, 1 μM NPS-2143, 0.002 % GDN, and 0.0002 % CHS were pooled and concentrated to approximately 5 mg ml^{-1} for further cryo-EM sample preparation.

Purification of active state CaSR bound to cinacalcet and TNCA

Infected cells (described above) were collected and resuspended in hypotonic buffer (20 mM HEPES pH 7.5, 10 mM NaCl, 10 mM $CaCl_2$, 10 % glycerol, 1× cocktail of protease inhibitor, 1 μM cinacalcet, and 1 μM TNCA). Cell membrane was collected by ultra-centrifugation at 40,000 r.p.m. for 1 hr, resuspended, and solubilized in buffer containing 20 mM HEPES, 150 mM NaCl, 10 mM $CaCl_2$, 10 % glycerol, 1 μM cinacalcet, 1 μM TNCA, 1 % LMNG, and 0.1 % CHS for 1 hr at 4 °C. The supernatant was collected by ultra-centrifugation and applied to an anti-Flag M2 antibody affinity column. After receptor binding to the M2 column, the resin was washed with 20 mM HEPES, 150 mM NaCl, 10 mM $CaCl_2$, 10 % glycerol, 1 μM cinacalcet, 1 μM TNCA, 0.1 % LMNG, 0.01 % CHS. LMNG was exchanged for GDN to a proportion of 0.2 % in stepwise washing. CaSR was then eluted with 20 mM HEPES, 150 mM NaCl, 10 mM $CaCl_2$, 10 % glycerol, 1 μM cinacalcet, 1 μM TNCA, 0.02 % GDN, 0.002 % CHS, and 0.2 mg ml^{-1} Flag peptide.

CaSR was further purified by Mono Q 5/50 GL column. Peak fractions were assembled and injected to a Superose 6 Increase 10/300 GL column. Fractions of CaSR in buffer containing 20 mM HEPES, 150 mM NaCl, 10 mM $CaCl_2$, 1 μM cinacalcet, 1 μM TNCA, 0.002 % GDN, and 0.0002 % CHS were pooled and concentrated to approximately 5 mg ml^{-1} for further cryo-EM sample preparation.

Cryo-EM sample preparation and data acquisition

Three microliters of inactive or active CaSR protein was applied to glow-discharged holey carbon 300 mesh grids (Quantifoil Au R1.2/1.3, Quantifoil MicroTools), respectively. The grids were blotted for 2 s and flash-frozen in liquid ethane using a Vitrobot Mark IV (Thermo Fisher Scientific) at 4 °C and 100 % humidity. Cryo-EM data was collected on a Titan Krios microscope (Thermo Fisher Scientific) at 300 kV accelerating voltage equipped with a Gatan K3 Summit direct election detector at a nominal magnification of 81,000× in counting mode at a pixel size of 1.071 Å. Each micrograph contains 36 movie frames with a total accumulated dose of 70 electrons per Å. The defocus range was set –1.5 to –2.5 μm. A total of 5706 and 4981 movies for active and inactive CaSR were collected for further data processing, respectively.

Data processing and 3D reconstruction

All images were aligned and summed using MotionCor2 (***Zheng et al., 2017***). Unless otherwise specified, single-particle analysis was mainly executed in RELION 3.1 (***Zivanov et al., 2020***). After CTF parameter determination using CTFFIND4 (***Rohou and Grigorieff, 2015***), particle auto-picking, manual particle checking, and reference-free 2D classification, 1,546,992 and 2,208,402 particles remained in the active and inactive datasets, respectively. The particles were extracted on a binned dataset with a pixel size of 4.42 Å and subjected to 3D classification, with the initial model generated by ab-initio reconstruction in cryoSPARC (***Punjani et al., 2017***).

For the CaSR active state dataset, 3D classification resulted in extraction of 36.6 % good particles with a pixel size of 1.071 Å. The particles were subsequently subjected to an auto-refine procedure, yielding a 4.3-Å-resolution map. Afterwards, particles were polished, sorted by carrying out multiple rounds of 3D classifications, yielding a dataset with 560,366 particles, generating a 3.3-Å-resolution map. Another round of 3D classification focusing the alignment on the complex, resulted in two conformations with high-quality features. After refinement, the resolution levels of these two

maps improved to 3.43 Å and 2.99 Å. Particle subtractions on the ECD and TM domains were also performed to further improve the map quality. After several rounds of 3D classifications, ECD map has a resolution of 3.07 Å with 493,869 particles, while that for TM is 4.3 Å with 389,105 particles.

For the CaSR inactive state dataset, 3D classification resulted in extraction of 55 % good particles with a pixel size of 1.071 Å. The particles were subsequently subjected to an auto-refine procedure, yielding a 6.0-Å-resolution map. Afterwards, particles were further sorted with another round of 3D classification focusing the alignment on the TM domain, resulted in 37.7 % particles with high-quality features. Further 3D classification on the whole complex separates three different orientations of ECD relative to TM domain. After refinement, the resolution levels of these three maps improved to 5.79 Å, 6.88 Å, and 7.11 Å. Particle subtractions on the ECD and TM domains were also performed to further improve the map quality. After several rounds of 3D classifications, ECD map has a resolution of 4.5 Å with 253,294 particles, while that for TM is 4.8 Å with 691,246 particles.

Model building and refinement

The crystal structures of CaSR ECD in apo and active forms (PDB Code: 5K5T, 5K5S) were used as initial templates for the ECD of the CaSR. The cryo-EM structures of mGluR5 in resting and active forms (PDB Code: 6N52, 6N51) were used as initial models for the TM domains of the receptor. The agonist TNCA was generated by COOT (***Emsley and Cowtan, 2004***) and PHENIX.eLBOW (***Adams et al., 2010***). The initial templates of ECDs and TMDs were docked into the cryo-EM maps of CaSR using UCSF Chimera (***Goddard et al., 2018***) to build the initial models of CaSR in inactive and active forms. Then the main chains and side chains of the initial models were manually rebuilt in COOT. The models were subsequently performed by real-time refinement in PHENIX.

Intracellular Ca^{2+} flux assay

HEK293T cells (ATCC) were transiently transfected with wild-type or mutant full-length CaSR plasmids. Five micrograms DNA plasmid was incubated with 15 µl lipofectimin in 500 µl OptiMEM for 10 min at room temperature and then added to the cells for overnight incubation at 37 °C. The transfected cells were trypsinized and seeded in 96-well plates. On the day of assay, the cells were incubated with loading medium containing 20 mM HEPES, 125 mM NaCl, 4 mM KCl, 1.25 mM $CaCl_2$, 1 mM $MgSO_4$,1 mM Na_2HPO_4, 0.1% D-glucose, and 0.1% BSA at 37°C for 4 hr. Then the buffer was replaced with 100 µl of buffer containing Fluo-4 at 37°C for 1 hr incubation, and then placed into the FLIPR Tetra High Throughput Cellular Screening System. Data was analyzed by non-linear regression in Prism (GraphPad Software). Data points represent average ± SEM of quadruplicate measurements.

Surface plasmon resonance

SPR experiments were performed using a Biacore T200 instrument (GE Healthcare). The system was flushed with running buffer (20 mM HEPES pH 7.4, 150 mM NaCl, 0.05 % Tween 20), and all steps were performed at 25 °C chip temperature. The CaSR ECD flowed through the negatively charged chip at a concentration of 1 mg/ml and a flow rate of 10 µl/min for 1 min and was captured by amino-carboxyl coupling reaction. It was followed by nanobody NB-2D11 that went through the chip at a series of concentration (30 µl/min, association: 90 s, dissociation: 220 s). All Biacore kinetic experiment data were obtained using Biacore S200 Evaluation Software to calculate the K_D, which is the ratio of *kd*/*ka*.

ELISA for cell-surface expression

ELISA was performed as a control to quantify cell surface expression of each CaSR mutant (***Mos et al., 2019***). In brief, HEK293T cells were transiently transfected with wild-type (WT) or mutant full-length CaSR plasmids. Five micrograms DNA plasmid was incubated with 15 µl lipofectimine (Invitrogen) in 500 µl OptiMEM (Gibco) for 10 min at room temperature and then added to the cells for overnight incubation at 37°C. The transfected cells were trypsinized and seeded in poly-D-lysine-coated 96-well plates (Greiner bio-one, cat# 655083). On the day of assay, cells were fixed with 4 % paraformaldehyde in PBS for 20 min and washed twice. The cells were incubated with blocking buffer containing 3 % skim milk in PBS followed by incubation for 1 hr with anti-Flag antibody (Yeasen) in blocking buffer. The cells were then incubated with horseradish peroxidase goat anti-mouse IgG (Yeasen) diluted 1:5000 in blocking solution for 1 hr. Chemiluminescence was measured on a Tecan plate reader immediately

after addition of 10 µl/well SuperSignal ELISA Femto Substrate (Thermo Fisher Scientific). The results show that each CaSR mutant displays similar fluorescence intensity as that of wild type, which indicates that the elimination of the calcium response is not caused by misfolding or mis-trafficking of the receptor. All mutants were well-expressed on the cell surface compared to the WT receptor.

Acknowledgements

The cryo-EM data were collected at the Cryo-Electron Microscopy Research Center, Shanghai Institute of Materia Medica, Chinese Academy of Sciences. This work is supported by National Natural Science Foundation of China (No. 31670743), Strategic Priority Research Program of the Chinese Academy of Sciences (No. XDA12040326), Science and Technology Commission of Shanghai Municipality (No. 18JC1415400), Joint Research Fund for Overseas, Hong Kong and Macao Scholars (No. 81628013), Natural Science Foundation of Shanghai (16ZR1442900), National Science Foundation for Young Scholar projects (118180359901), and grants from Shanghai Institute of Materia Medica, Chinese Academy of Sciences (CASIMM0120164013, SIMM1606YZZ-06, SIMM1601KF-06, 55201631121116101, 55201631121108000, 5112345601, 2015123456005).

Additional information

Funding

Funder	Grant reference number	Author
National Natural Science Foundation of China	No. 31670743	Yong Geng
Science and Technology Commission of Shanghai Municipality	No. 18JC1415400	Yong Geng
Joint Research Fund for Overseas Chinese Scholars and Scholars in Hong Kong and Macao	No. 81628013	Yong Geng
Natural Science Foundation of Shanghai	16ZR1442900	Yong Geng
Shanghai Institute of Materia Medica, Chinese Academy of Sciences	CASIMM0120164013	Yong Geng
Shanghai Institute of Materia Medica, Chinese Academy of Sciences	SIMM1606YZZ-06	Yong Geng
Shanghai Institute of Materia Medica, Chinese Academy of Sciences	SIMM1601KF-06	Yong Geng
Shanghai Institute of Materia Medica, Chinese Academy of Sciences	55201631121116101	Yong Geng
Shanghai Institute of Materia Medica, Chinese Academy of Sciences	55201631121108000	Yong Geng
Shanghai Institute of Materia Medica, Chinese Academy of Sciences	5112345601	Yong Geng
Shanghai Institute of Materia Medica, Chinese Academy of Sciences	2015123456005	Yong Geng

Funder	Grant reference number	Author
National Natural Science Foundation of China	118180359901	Yong Geng

The funders had no role in study design, data collection and interpretation, or the decision to submit the work for publication.

Author contributions

Xiaochen Chen, Data curation, Formal analysis, Investigation, Methodology, Project administration, Validation, Visualization, Writing – original draft, Writing – review and editing; Lu Wang, Data curation, Investigation, Validation, Writing – original draft, Writing – review and editing; Qianqian Cui, Investigation, Writing – review and editing; Zhanyu Ding, Data curation, Investigation, Validation, Writing – original draft; Li Han, Yongjun Kou, Wenqing Zhang, Haonan Wang, Xiaomin Jia, Mei Dai, Zhenzhong Shi, Yuying Li, Xiyang Li, Investigation; Yong Geng, Conceptualization, Data curation, Formal analysis, Funding acquisition, Investigation, Methodology, Project administration, Resources, Supervision, Validation, Visualization, Writing – original draft

Author ORCIDs

Xiaochen Chen http://orcid.org/0000-0002-0426-9547
Lu Wang http://orcid.org/0000-0001-6336-5806
Qianqian Cui http://orcid.org/0000-0002-5962-9298
Zhanyu Ding http://orcid.org/0000-0002-8136-2243
Yong Geng http://orcid.org/0000-0001-7144-3878

Ethics

The animal work was approved and under the supervision of Shanghai Institute of Materia Medica, Chinese Academy of Sciences (Permit Number: SYXK 2015-0027).

Decision letter and Author response

Decision letter https://doi.org/10.7554/eLife.68578.sa1
Author response https://doi.org/10.7554/eLife.68578.sa2

Additional files

Supplementary files

- Transparent reporting form

Data availability

All data is available in the main text or the supplementary materials. Cryo-EM maps of active CaSR in complex with TNCA and inactive CaSR in complex with NB-2D11 have been deposited in the Electron Microscopy Data Bank under accession codes: EMD-30997 (NB-2D11 bound CaSR), EMD-30996 (TNCA bound CaSR). Atomic coordinates for the CaSR in complex with TNCA or NB-2D11 have been deposited in the Protein Data Bank under accession codes: 7E6U (NB-2D11 bound CaSR), 7E6T (TNCA bound CaSR).

The following dataset was generated:

Author(s)	Year	Dataset title	Dataset URL	Database and Identifier
Geng Y, Chen XC	2021	Cryo-EM structure of CaSR in complex with NB-2D11	http://www.rcsb.org/structure/unreleased/7E6U	RCSB Protein Data Bank, 7E6U
Chen X, Wang L, Ding Z, Cui Q, Han L, Kou Y, Zhang W, Wang H, Jia X, Dai M, Shi Z, Li Y, Li X, Geng Y	2021	Cryo-EM structure of CaSR in complex with TNCA	http://www.rcsb.org/structure/unreleased/7E6T	RCSB Protein Data Bank, 7E6T

The following previously published datasets were used:

Author(s)	Year	Dataset title	Dataset URL	Database and Identifier
Geng Y, Mosyak L, Kurinov I, Zuo H, Sturchler E, Cheng TC, Subramanyam P, Brown AP, Brennan SC, Mun H-C, Bush M, Chen Y, Nguyen T, Cao B, Chang D, Quick M, Conigrave A, Colecraft HM, McDonald P, Fan QR	2016	Crystal structure of the inactive form of human calcium-sensing receptor extracellular domain	https://www.rcsb.org/structure/5K5T	RCSB Protein Data Bank, 5K5T
Geng Y, Mosyak L, Kurinov I, Zuo H, Sturchler E, Cheng TC, Subramanyam P, Brown AP, Brennan SC, Mun H-C, Bush M, Chen Y, Nguyen T, Cao B, Chang D, Quick M, Conigrave A, Colecraft HM, McDonald P, Fan QR	2016	Crystal structure of the active form of human calcium-sensing receptor extracellular domain	https://www.rcsb.org/structure/5K5S	RCSB Protein Data Bank, 5K5S
Koehl A, Hu H, Feng D, Sun B, Weis WI, Skiniotis GS, Mathiesen JM, Kobilka BK	2019	Metabotropic Glutamate Receptor 5 bound to L-quisqualate and Nb43	https://www.rcsb.org/structure/6N51	RCSB Protein Data Bank, 6N51
Mao C, Shen C, Li C, Shen D, Xu C, Zhang S, Zhou R, Shen Q, Chen L, Jiang Z, Liu J, Zhang Y	2020	Cryo-EM structure of the baclofen/BHFF-bound human GABA(B) receptor in active state	https://www.rcsb.org/structure/7C7Q	RCSB Protein Data Bank, 7C7Q

References

Adams PD, Afonine PV, Bunkoczi G, Chen VB, Davis IW, Echols N, Headd JJ, Hung LW, Kapral GJ, Grosse-Kunstleve RW. 2010. PHENIX: a comprehensive Python-based system for macromolecular structure solution. *Acta Crystallographica Section D, Biological Crystallography* **66**: 213–221. DOI: https://doi.org/10.1107/S0907444909052925, PMID: 20124702

Alexander ST, Hunter T, Walter S, Dong J, Maclean D, Baruch A, Subramanian R, Tomlinson JE. 2015. Critical Cysteine Residues in Both the Calcium-Sensing Receptor and the Allosteric Activator AMG 416 Underlie the Mechanism of Action. *Molecular Pharmacology* **88**: 853–865. DOI: https://doi.org/10.1124/mol.115.098392, PMID: 26290606

Brown EM, Gamba G, Riccardi D, Lombardi M, Butters R, Kifor O, Sun A, Hediger MA, Lytton J, Hebert SC. 1993. Cloning and characterization of an extracellular Ca(2+)-sensing receptor from bovine parathyroid. *Nature* **366**: 575–580. DOI: https://doi.org/10.1038/366575a0, PMID: 8255296

Brown EM. 2013. Role of the calcium-sensing receptor in extracellular calcium homeostasis. *Best Practice & Research Clinical Endocrinology & Metabolism* **27**: 333–343. DOI: https://doi.org/10.1016/j.beem.2013.02.006

Centeno PP, Herberger A, Mun HC, Tu C, Nemeth EF, Chang W, Conigrave AD, Ward DT. 2019. Phosphate acts directly on the calcium-sensing receptor to stimulate parathyroid hormone secretion. *Nature Communications* **10**: 4693. DOI: https://doi.org/10.1038/s41467-019-12399-9, PMID: 31619668

Chang W, Tu CL, Jean-Alphonse FG, Herberger A, Cheng Z, Hwong J, Ho H, Li A, Wang D, Liu H. 2020. PTH hypersecretion triggered by a GABAB1 and Ca(2+)-sensing receptor heterocomplex in hyperparathyroidism. *Nature Metabolism* **2**: 243–255. DOI: https://doi.org/10.1038/s42255-020-0175-z, PMID: 32694772

Conigrave AD, Quinn SJ, Brown EM. 2000. L-amino acid sensing by the extracellular Ca2+-sensing receptor. *PNAS* **97**: 4814–4819. DOI: https://doi.org/10.1073/pnas.97.9.4814, PMID: 10781086

Conigrave AD, Mun HC, Delbridge L, Quinn SJ, Wilkinson M, Brown EM. 2004. L-amino acids regulate parathyroid hormone secretion. *The Journal of Biological Chemistry* **279**: 38151–38159. DOI: https://doi.org/10.1074/jbc.M406373200, PMID: 15234970

Ellaithy A, Gonzalez-Maeso J, Logothetis DA, Levitz J. 2020. Structural and Biophysical Mechanisms of Class C G Protein-Coupled Receptor Function. *Trends in Biochemical Sciences* **45**: 1049–1064. DOI: https://doi.org/10.1016/j.tibs.2020.07.008, PMID: 32861513

Emsley P, Cowtan K. 2004. Coot: model-building tools for molecular graphics. *Acta Crystallographica Section D, Biological Crystallography* **60**: 2126–2132. DOI: https://doi.org/10.1107/S0907444904019158, PMID: 15572765

Geng Y, Bush M, Mosyak L, Wang F, Fan QR. 2013. Structural mechanism of ligand activation in human GABA(B) receptor. *Nature* **504**: 254–259. DOI: https://doi.org/10.1038/nature12725, PMID: 24305054

Geng Y, Mosyak L, Kurinov I, Zuo H, Sturchler E, Cheng TC, Subramanyam P, Brown AP, Brennan SC, Mun HC. 2016. Structural mechanism of ligand activation in human calcium-sensing receptor. *eLife* **5**: e13662. DOI: https://doi.org/10.7554/eLife.13662, PMID: 27434672

Goddard TD, Huang CC, Meng EC, Pettersen EF, Couch GS, Morris JH, Ferrin TE. 2018. UCSF ChimeraX: Meeting modern challenges in visualization and analysis. *Protein Science* **27**: 14–25. DOI: https://doi.org/10.1002/pro.3235, PMID: 28710774

Goehring A, Lee CH, Wang KH, Michel JC, Claxton DP, Baconguis I, Althoff T, Fischer S, Garcia KC, Gouaux E. 2014. Screening and large-scale expression of membrane proteins in mammalian cells for structural studies. *Nature Protocols* **9**: 2574–2585. DOI: https://doi.org/10.1038/nprot.2014.173, PMID: 25299155

Hannan FM, Kallay E, Chang W, Brandi ML, Thakker RV. 2018. The calcium-sensing receptor in physiology and in calcitropic and noncalcitropic diseases. *Nature Reviews Endocrinology* **15**: 33–51. DOI: https://doi.org/10.1038/s41574-018-0115-0, PMID: 30443043

Heaney CF, Kinney JW. 2016. Role of GABA(B) receptors in learning and memory and neurological disorders. *Neuroscience and Biobehavioral Reviews* **63**: 1–28. DOI: https://doi.org/10.1016/j.neubiorev.2016.01.007, PMID: 26814961

Hendy GN, Guarnieri V, Canaff L. 2009. Calcium-sensing receptor and associated diseases. *Progress in Molecular Biology and Translational Science* **89**: 31–95. DOI: https://doi.org/10.1016/S1877-1173(09)89003-0, PMID: 20374733

Hofer AM, Brown EM. 2003. Extracellular calcium sensing and signalling. *Nature Reviews. Molecular Cell Biology* **4**: 530–538. DOI: https://doi.org/10.1038/nrm1154, PMID: 12838336

Jensen AA, Brauner-Osborne H. 2007. Allosteric modulation of the calcium-sensing receptor. *Current Neuropharmacology* **5**: 180–186. DOI: https://doi.org/10.2174/157015907781695982, PMID: 19305800

Kim Y, Jeong E, Jeong JH, Kim Y, Cho Y. 2020. Structural Basis for Activation of the Heterodimeric GABAB Receptor. *Journal of Molecular Biology* **432**: 5966–5984. DOI: https://doi.org/10.1016/j.jmb.2020.09.023, PMID: 33058878

Koehl A, Hu H, Feng D, Sun B, Zhang Y, Robertson MJ, Chu M, Kobilka TS, Laeremans T, Steyaert J. 2019. Structural insights into the activation of metabotropic glutamate receptors. *Nature* **566**: 79–84. DOI: https://doi.org/10.1038/s41586-019-0881-4, PMID: 30675062

Kunishima N, Shimada Y, Tsuji Y, Sato T, Yamamoto M, Kumasaka T, Nakanishi S, Jingami H, Morikawa K. 2000. Structural basis of glutamate recognition by a dimeric metabotropic glutamate receptor. *Nature* **407**: 971–977. DOI: https://doi.org/10.1038/35039564, PMID: 11069170

Leach K, Gregory KJ, Kufareva I, Khajehali E, Cook AE, Abagyan R, Conigrave AD, Sexton PM, Christopoulos A. 2016. Towards a structural understanding of allosteric drugs at the human calcium-sensing receptor. *Cell Research* **26**: 574–592. DOI: https://doi.org/10.1038/cr.2016.36, PMID: 27002221

Levitz J, Habrian C, Bharill S, Fu Z, Vafabakhsh R, Isacoff EY. 2016. Mechanism of Assembly and Cooperativity of Homomeric and Heteromeric Metabotropic Glutamate Receptors. *Neuron* **92**: 143–159. DOI: https://doi.org/10.1016/j.neuron.2016.08.036, PMID: 27641494

Ling S, Shi P, Liu S, Meng X, Zhou Y, Sun W, Chang S, Zhang X, Zhang L, Shi C. 2021. Structural mechanism of cooperative activation of the human calcium-sensing receptor by Ca(2+) ions and L-tryptophan. *Cell Research* **31**: 383–394. DOI: https://doi.org/10.1038/s41422-021-00474-0, PMID: 33603117

Liu H, Yi P, Zhao W, Wu Y, Acher F, Pin JP, Liu J, Rondard P. 2020. Illuminating the allosteric modulation of the calcium-sensing receptor. *PNAS* **117**: 21711–21722. DOI: https://doi.org/10.1073/pnas.1922231117, PMID: 32817431

Manglik A, Kim TH, Masureel M, Altenbach C, Yang Z, Hilger D, Lerch MT, Kobilka TS, Thian FS, Hubbell WL. 2015. Structural Insights into the Dynamic Process of beta2-Adrenergic Receptor Signaling. *Cell* **161**: 1101–1111. DOI: https://doi.org/10.1016/j.cell.2015.04.043, PMID: 25981665

Mao C, Shen C, Li C, Shen DD, Xu C, Zhang S, Zhou R, Shen Q, Chen LN, Jiang Z. 2020. Cryo-EM structures of inactive and active GABAB receptor. *Cell Research* **30**: 564–573. DOI: https://doi.org/10.1038/s41422-020-0350-5, PMID: 32494023

Mos I, Jacobsen SE, Foster SR, Brauner-Osborne H. 2019. Calcium-Sensing Receptor Internalization Is beta-Arrestin-Dependent and Modulated by Allosteric Ligands. *Molecular Pharmacology* **96**: 463–474. DOI: https://doi.org/10.1124/mol.119.116772, PMID: 31399503

Muto T, Tsuchiya D, Morikawa K, Jingami H. 2007. Structures of the extracellular regions of the group II/III metabotropic glutamate receptors. *PNAS* **104**: 3759–3764. DOI: https://doi.org/10.1073/pnas.0611577104, PMID: 17360426

Nemeth EF, Heaton WH, Miller M, Fox J, Balandrin MF, Van Wagenen BC, Colloton M, Karbon W, Scherrer J, Shatzen E. 2004. Pharmacodynamics of the type II calcimimetic compound cinacalcet HCl. *The Journal of Pharmacology and Experimental Therapeutics* **308**: 627–635. DOI: https://doi.org/10.1124/jpet.103.057273, PMID: 14593085

Papasergi-Scott MM, Robertson MJ, Seven AB, Panova O, Mathiesen JM, Skiniotis G. 2020. Structures of metabotropic GABAB receptor. *Nature* **584**: 310–314. DOI: https://doi.org/10.1038/s41586-020-2469-4, PMID: 32580208

Pardon E, Laeremans T, Triest S, Rasmussen SG, Wohlkonig A, Ruf A, Muyldermans S, Hol WG, Kobilka BK, Steyaert J. 2014. A general protocol for the generation of Nanobodies for structural biology. *Nature Protocols* **9**: 674–693. DOI: https://doi.org/10.1038/nprot.2014.039, PMID: 24577359

Park J, Fu Z, Frangaj A, Liu J, Mosyak L, Shen T, Slavkovich VN, Ray KM, Taura J, Cao B. 2020. Structure of human GABAB receptor in an inactive state. *Nature* **584**: 304–309. DOI: https://doi.org/10.1038/s41586-020-2452-0, PMID: 32581365

Pin JP, Bettler B. 2016. Organization and functions of mGlu and GABAB receptor complexes. *Nature* **540**: 60–68. DOI: https://doi.org/10.1038/nature20566, PMID: 27905440

Pollak MR, Brown EM, Chou YH, Hebert SC, Marx SJ, Steinmann B, Levi T, Seidman CE, Seidman JG. 1993. Mutations in the human Ca(2+)-sensing receptor gene cause familial hypocalciuric hypercalcemia and neonatal severe hyperparathyroidism. *Cell* **75**: 1297–1303. DOI: https://doi.org/10.1016/0092-8674(93)90617-y, PMID: 7916660

Punjani A, Rubinstein JL, Fleet DJ, Brubaker MA. 2017. cryoSPARC: algorithms for rapid unsupervised cryo-EM structure determination. *Nature Methods* **14**: 290–296. DOI: https://doi.org/10.1038/nmeth.4169, PMID: 28165473

Quinn SJ, Bai M, Brown EM. 2004. pH Sensing by the calcium-sensing receptor. *The Journal of Biological Chemistry* **279**: 37241–37249. DOI: https://doi.org/10.1074/jbc.M404520200, PMID: 15201280

Rey O, Young SH, Yuan J, Slice L, Rozengurt E. 2005. Amino acid-stimulated Ca2+ oscillations produced by the Ca2+-sensing receptor are mediated by a phospholipase C/inositol 1,4,5-trisphosphate-independent pathway that requires G12, Rho, filamin-A, and the actin cytoskeleton. *The Journal of Biological Chemistry* **280**: 22875–22882. DOI: https://doi.org/10.1074/jbc.M503455200, PMID: 15837785

Rohou A, Grigorieff N. 2015. CTFFIND4: Fast and accurate defocus estimation from electron micrographs. *Journal of Structural Biology* **192**: 216–221. DOI: https://doi.org/10.1016/j.jsb.2015.08.008, PMID: 26278980

Rosenbaum DM, Zhang C, Lyons JA, Holl R, Aragao D, Arlow DH, Rasmussen SG, Choi HJ, Devree BT, Sunahara RK. 2011. Structure and function of an irreversible agonist-beta(2) adrenoceptor complex. *Nature* **469**: 236–240. DOI: https://doi.org/10.1038/nature09665, PMID: 21228876

Saidak Z, Boudot C, Abdoune R, Petit L, Brazier M, Mentaverri R, Kamel S. 2009. Extracellular calcium promotes the migration of breast cancer cells through the activation of the calcium sensing receptor. *Experimental Cell Research* **315**: 2072–2080. DOI: https://doi.org/10.1016/j.yexcr.2009.03.003, PMID: 19285978

Shaye H, Ishchenko A, Lam JH, Han GW, Xue L, Rondard P, Pin JP, Katritch V, Gati C, Cherezov V. 2020. Structural basis of the activation of a metabotropic GABA receptor. *Nature* **584**: 298–303. DOI: https://doi.org/10.1038/s41586-020-2408-4, PMID: 32555460

Tsuchiya D, Kunishima N, Kamiya N, Jingami H, Morikawa K. 2002. Structural views of the ligand-binding cores of a metabotropic glutamate receptor complexed with an antagonist and both glutamate and Gd3+. *PNAS* **99**: 2660–2665. DOI: https://doi.org/10.1073/pnas.052708599, PMID: 11867751

Walter S, Baruch A, Dong J, Tomlinson JE, Alexander ST, Janes J, Hunter T, Yin Q, Maclean D, Bell G. 2013. Pharmacology of AMG 416 (Velcalcetide), a novel peptide agonist of the calcium-sensing receptor, for the treatment of secondary hyperparathyroidism in hemodialysis patients. *The Journal of Pharmacology and Experimental Therapeutics* **346**: 229–240. DOI: https://doi.org/10.1124/jpet.113.204834, PMID: 23674604

Ward BK, Magno AL, Walsh JP, Ratajczak T. 2012. The role of the calcium-sensing receptor in human disease. *Clinical Biochemistry* **45**: 943–953. DOI: https://doi.org/10.1016/j.clinbiochem.2012.03.034, PMID: 22503956

Xue L, Rovira X, Scholler P, Zhao H, Liu J, Pin JP, Rondard P. 2015. Major ligand-induced rearrangement of the heptahelical domain interface in a GPCR dimer. *Nature Chemical Biology* **11**: 134–140. DOI: https://doi.org/10.1038/nchembio.1711, PMID: 25503927

Young SH, Rozengurt E. 2002. Amino acids and ca2+ stimulate different patterns of ca2+ oscillations through the ca2+-sensing receptor. *American Journal of Physiology. Cell Physiology* **282**: C1414-C1422. DOI: https://doi.org/10.1152/ajpcell.00432.2001, PMID: 11997256

Zhang C, Zhang T, Zou J, Miller CL, Gorkhali R, Yang JY, Schilmiller A, Wang S, Huang K, Brown EM. 2016. Structural basis for regulation of human calcium-sensing receptor by magnesium ions and an unexpected tryptophan derivative co-agonist. *Science Advances* **2**: e1600241. DOI: https://doi.org/10.1126/sciadv.1600241, PMID: 27386547

Zheng SQ, Palovcak E, Armache JP, Verba KA, Cheng Y, Agard DA. 2017. MotionCor2: anisotropic correction of beam-induced motion for improved cryo-electron microscopy. *Nature Methods* **14**: 331–332. DOI: https://doi.org/10.1038/nmeth.4193, PMID: 28250466

Zivanov J, Nakane T, Scheres SHW. 2020. Estimation of high-order aberrations and anisotropic magnification from Cryo-em data sets in relion-3.1. *IUCrJ* **7**: 253–267. DOI: https://doi.org/10.1107/s2052252520000081, PMID: 32148853